Electrical Control of the Transduction Channels' Gating Force in Mechanosensory Hair Cells.

*Achille Joliot, Laure Stickel and Pascal Martin**

A. Joliot, L. Stickel, P. Martin

Physique des Cellules et Cancer, Institut Curie—PSL Research University, CNRS, Sorbonne Université, F-75248 Paris, France.

email: pascal.martin@curie.fr

Funding:

Fondation pour l'Audition grant FPA RD 2020-7 (PM)

Labex Cell(n)Scale grant ANR-11-LABX-0038 (PM)

Labex Cell(n)Scale grant ANR-10-IDEX-001-02 (PM)

Université Paris Sciences et Lettres and doctoral school "Physique en Île-de-France" grant (AJ)

Keywords: auditory system, bioelectricity, gating compliance, mechanosensitive ion channels, vestibular system.

Abstract

The inner ear's hair cells rely on mechanosensitive ion channels to convert vibrations of their hair bundles into electrical signals. The mechanical correlates of channel gating—the gating force and the gating swing—are fundamental determinants of hair-cell mechanosensitivity but are still poorly understood. Here we show that varying the electrical potential across the sensory hair-cell epithelium continuously modulates the gating force, by up to $\pm 100\%$. Our observations also revealed an abrupt transition between states of weak and strong gating force at a threshold potential, so that strong gating forces associated to high mechanosensitivity are observed only when the calcium influx through the channels is large enough, but not too large. Gating-force changes, remarkably enough, were explained by the modulability of the gating swing, ranging from values comparable to the channel pore size to nearly tenfold larger. Gating-swing control is expected to underly the hair cell's ability to tune its mechanosensitivity to minute sound stimuli.

1. Introduction

Mechanoreception by the inner ear's sensory hair cells begins with the deflection of their hair bundle—a cohesive tuft of cylindrical stereocilia arranged in a staircase pattern.[1–3] A deflection toward the taller row of stereocilia increases mechanical tension in oblique tip links, which connect the tip of each stereocilium to the flank of a taller neighbor. The increased tip-link tension opens mechanosensitive ion channels and evokes an influx of cations into the hair cell, primarily K^+ ions but also Ca^{2+} ions.

Our understanding of hair-cell mechanosensitivity is informed by the gating-spring model of mechanoelectrical transduction.[4,5] Within this framework, the transduction channels are gated directly by force, which is transmitted to the channels via elastic elements—the gating springs—that operate in series with the tip links. The product of the gating-spring stiffness and the gating swing defines the gating force, a fundamental determinant of hair-cell mechanosensitivity: its magnitude sets the maximal slope of the sigmoidal relation between the transduction current and the deflection of the hair bundle (Figure S1A,B, Supporting Information). The greater the gating force, the larger the transduction current evoked by a small stimulus, making the hair cell more sensitive to a given deflection of its hair bundle.

The gating-spring model imposes a reciprocal relationship between tip-link tension and channel gating. If tensioning the tip links evokes channel opening, then channel opening must reduce tip-link tension by an amount given precisely by the gating force. Feedback between tip-link tension and channel gating produces gating compliance, the effective softening of the hair bundle upon channel gating.[6,7] For large positive or negative bundle displacements, at which the transduction channels are nearly all open or closed, respectively, the force-displacement relation is linear. At intermediate displacements that elicit channel gating, however, the slope of the force-displacement relation is reduced: the hair bundle is effectively softer. Gating compliance is associated with a shift between the two linear limbs of the force-displacement relation; this shift provides an estimate of the combined gating force, denoted F_G in the following, produced by the ensemble of transduction channels that operate in parallel within the hair bundle (Figure S1B, Supporting Information). Furthermore, upon an oscillatory movement of the hair bundle, opening and closing of the transduction channels also increase friction on the hair bundle, a phenomenon called gating friction.[8] The experimental demonstration of gating compliance and gating friction at the cellular scale of a micron-sized hair bundle provides strong support for the gating-spring model. Because these phenomena

reflect the mechanical correlate of channel gating, they can also be used to infer fundamental properties of channel gating at the molecular scale such as the gating force.[6,7,9]

Biophysical estimates of the gating force are variable, even with hair cells from the same animal species and organ. With hair cells in excised preparations of the mammalian cochlea, there is some evidence of gating compliance [10–14] but gating forces can also be so weak that the force-displacement relation remains linear.[15–17] In these experiments, however, the endocochlear potential that normally boosts transduction currents in vivo is absent and the hair cells are fully immersed in a standard extracellular fluid called perilymph, which is rich in Na^+ and with a Ca^{2+} concentration in the millimolar range. This condition disrupts the two ionic compartments that hair cells experience in vivo, with endolymph—an unusual K^+-rich fluid with a low Ca^{2+} concentration (20-250 μM)—and perilymph bathing the cells' apical and basal aspects, respectively. In addition, because cochlear hair bundles are weakly cohesive, gating-force estimates depend on the method of mechanical stimulation [17,18] and where displacement is measured within the bundle.[19]

The frog saccule has provided a robust model system to study gating forces. Hair bundles are highly cohesive, which ensures concerted gating of the transduction channels of their hair bundles.[20,21] In addition, because adaptation is relatively slow, the effects of channel gating on hair-bundle mechanics can be evaluated before adaptation kicks in and obscures the interpretation of force measurements.[9] Finally, the organ can be mounted in a two-chamber configuration, which allows to mimic the natural ionic conditions. [22,23] With frog saccular hair cells, gating forces can lead to a moderate (about 40%) decrease in hair-bundle stiffness [6] or be strong enough to result in negative stiffness, which can lead to spontaneous oscillations of the hair bundle and, in turn, frequency-selective amplification of periodic stimuli.[9,23–25] Remarkably enough, strong gating forces and negative stiffness were reported only under ex-vivo conditions that closely mimic natural ones, with reconstituted endolymph-perilymph compartments. This and other circumstantial evidence [26,27] suggests that the magnitude of the gating force may vary with the Ca^{2+} concentration in the fluid bathing the hair bundle.

In this work, we clarify the apparent variability of the gating force by providing a comprehensive and systematic investigation of the mechanical correlates of channel gating in hair-bundle mechanics under a range of conditions. We report that the electrical potential across the sensory epithelium that houses the hair cells can serve as a control parameter of the gating force. Our results indicate that the gating force varies primarily because the gating swing varies.

98 Our work further reveals a reversible, but hysteretic, transition between a state of strong gating
99 force, for which the hair bundles oscillate spontaneously, and a state of weak gating force, for
100 which hair-bundle mechanics is linear and the hair bundles are quiescent. We finally provide
101 evidence that these effects are mediated, at least in part, by electrical control of the influx of
102 Ca^{2+} through the transduction channels.

103 **2. Results**

104 We took advantage of an excised preparation of the frog saccule that mimics *ex vivo* the two-
105 compartment ionic conditions that the sensory epithelium experiences *in vivo*. Under these
106 conditions, the hair cells routinely displayed spontaneous oscillations of their hair bundles, as
107 recognized before.[26,28,29] We aimed here at evaluating the effects of a transepithelial potential
108 on hair-bundle mechanics. To this end, we used a pair of electrodes and a current generator to
109 impose a transepithelial current, I, within a range of ± 10 μA (**Figure** 1A). Upon application of
110 a current step, the transepithelial potential changed with a time course that was well described
111 by an exponential relation with a characteristic timescale of 230 ± 50 μs (mean $\pm$ SD, n =13;
112 Figure 1B). The transepithelial potential thus reached a steady-state value, noted U in the
113 following, in about 600 μs. Over an ensemble of 13 saccules, we found a transepithelial
114 resistance of 10 ± 2 kΩ (mean $\pm$ SD). Thus, a positive current of $+1$ μA evoked a positive
115 potential in the endolymphatic compartment of about $+10$ mV with respect to the perilymphatic
116 compartment; accordingly, the transepithelial potential thus varied within a range of ± 100 mV.
117 We emphasize for the following that a positive endolymphatic potential is expected to increase
118 the influx of K^+ and Ca^{2+} ions through the transduction channels, whereas a negative potential
119 does the opposite. All numerical results are given below as the average and standard deviations
120 (SD) over an ensemble of n independent measurements.

121 **2.1 The potential modulates strongly the gating force but weakly the hair-bundle stiffness**

122 To determine the effects of an endolymphatic potential on the mechanical properties of a hair
123 bundle, we measured the bundle's force-displacement relation in response to a series of step
124 displacements applied to the base of a stimulus fiber (**Figure 2**). Under control conditions, for
125 which no transepithelial current was applied ($I = 0$), the force-displacement relation showed a
126 prominent region of reduced slope, or gating compliance, which is expected for hair bundles
127 that oscillate spontaneously.[9,24] A fit of the relation to Equation 1 (Experimental Section)
128 yielded a set-point deflection $X_0 = -2 \pm 7$ nm, a gating force $F_G = 17 \pm 4$ pN and a linear

stiffness $K = 0.85 \pm 0.2\ \mathrm{pN \cdot nm^{-1}}$ ($n = 29$ in 16 frogs). We recall that the set-point deflection can be interpreted as the deflection that leads to a channels' open probability of ½.[24] For each hair bundle, the procedure was repeated in the presence of a static transepithelial current ($I \neq 0$).

We start by presenting the effects of a transepithelial current on a force-displacement relation in four representative examples (Figure 2); the effects on the corresponding spontaneous hair-bundle oscillations are shown in Figure S2A-D (Supplementary Information). Applying a positive current, here $I = +3$ μA, corresponding to a positive endolymphatic potential $U \simeq +30$ mV, evoked an increase of the set-point deflection: the transduction channels closed (Figure 2A). In addition, we observed a small (-5%) decrease of the linear bundle's stiffness and, remarkably, a large decrease (-38%) of the gating force. In another cell, a larger current $I = +6$ μA resulted in a similar change in stiffness (-6%) but evoked a larger decrease of the gating force (-50%; Figure 2B). Conversely, applying a negative current of moderate magnitude, here $I = -3$ μA, corresponding to a negative endolymphatic potential $\mathrm{U} \simeq -30$ mV, elicited a decrease of the set-point deflection and thus opening of the transduction channels, a small increase ($+10\%$) of the linear stiffness, and a large increase ($+89\%$) of the gating force (Figure 2C). Furthermore, applying a large transepithelial current, here $\mathrm{I} = -6$ μA, led to an unexpected finding: the force-displacement relation became linear (Figure 2D). This is not because the integrity of the hair cell was impaired by application of a large transepithelial current, for all the effects were fully reversible.

Performing an ensemble of $n = 41$ pairs of measurements in 29 hair bundles from 16 frogs confirmed the effects illustrated by the four representative examples. We found a strong positive correlation between the change, $\Delta X_0 = X_0(I) - X_0(I = 0)$, of the set-point deflection and the applied transepithelial current (Pearson correlation $\mathrm{r} = 0.87$; p-value: $4 \cdot 10^{-11}$; $n = 34$; **Figure 3A**). This correlation came as no surprise, for the endolymphatic potential resulting from the transepithelial current should influence the magnitude of the Ca^{2+} influx through the transduction channels, and calcium is known to promote channel closure.[4,24,27,30,31] The change in linear stiffness, $\Delta K = K(I) - K(I = 0)$, was negatively correlated to the transepithelial current, but the correlation was weaker (Pearson correlation $\mathrm{r} = -0.57$; p-value: 10^{-4}; $n = 41$) (Figure 3B). Instead, for currents $I > -4$ μA, the change, $\Delta F_G = F_G(I) - F_G(I = 0)$, of the hair-bundle's gating force displayed a strong negative correlation with the current (Pearson correlation $\mathrm{r} = -0.86$; p-value: $8 \cdot 10^{-11}$; $n = 34$; Figure 3C). The relative variation of the

gating force was correspondingly much larger than that of the linear stiffness (Figure 3D). A positive transepithelial current evoked a reduction of the gating force by as much as -80%, whereas the stiffness decreased at most by -10% over the same range of transepithelial currents. Conversely, the gating force could nearly double in the presence of a negative transepithelial current, corresponding to a relative increase of $+100\%$, whereas stiffness did not increase beyond $+25\%$. These correlations between mechanical properties of the hair bundle and the transepithelial current were associated to systematic changes of the frequency, amplitude and waveform of spontaneous hair-bundle oscillations (Figure S2E-G, Supplementary Information).

For all the seven hair bundles for which the transepithelial current was more negative than -5 μA, corresponding to an endolymphatic potential $U \leq -50$ mV, the gating force did not follow the trend observed at more positive potentials. Instead of increasing further or saturating at more negative potentials, the gating force dropped to values so low that the force-displacement relation was linear, thus with no detectable signature of gating compliance (Figures 2D and 3C,D). At these endolymphatic potentials, no spontaneous oscillation was observed; the hair bundles were quiescent (Figure S2D, Supplementary Information). Our study thus revealed the existence of a critical value of the transepithelial current, $I = I_C \simeq -5\ \mu A$, and of the endolymphatic potential, $U = U_C \simeq -50$ mV, that delimited two functional states of the hair bundle: a state of strong gating force for which gating compliance was large enough to yield spontaneous oscillations of the hair bundle and a state of weak gating force for which hair-bundle mechanics was linear and the hair bundle was quiescent.

2.2 The gating force varies because the gating swing varies

Within the framework of the gating-spring model (Figure S1A, , Supplementary Information), the gating force for the whole hair bundle, $F_G = K_{GS}D$, is the product of the combined stiffness of the gating springs, K_{GS}, and of the gating swing, D, of a transduction channel. We note that this interpretation of the gating force rests on the tight cohesiveness of hair bundles in the frog saccule,[20,21] so that force directed to the transduction channels upon deflection of the bundle's tip is distributed evenly across tip links.[32] Remarkably enough, the relative effect of an endolymphatic potential on the gating force was much larger than that on the hair-bundle stiffness and could even be of opposite sign (Figure 3D). The contrast in behavior was particularly striking at the transition between regimes of strong and weak gating force ($I \leq I_C$). Although the gating force dropped to undetectable levels, the hair-bundle stiffness instead

showed a mild increased with respect to control conditions. Because the gating springs are expected to contribute a significant fraction of the total hair-bundle stiffness,[33] K, we reasoned that the change in gating force resulted mainly from a change in the magnitude of the gating swing. We could confirm this inference by measuring the hair-bundle stiffness, $K_{SP} = 0.17 \pm 0.03\ \mathrm{pN \cdot nm^{-1}}$ $(n = 14)$ $\simeq 0.2\ K$, after disruption of the tip links. By subtracting the average value of K_{SP} to individual measurements of K, we could then estimate, for each hair bundle, the gating-spring stiffness $K_{GS} = K - K_{SP}$, and in turn the gating swing D. After projection along the oblique axis of the tip links using the projection factor $\gamma = 0.14$,[32] we found a gating swing $d = \gamma D = 3.7 \pm 1.4\ \mathrm{nm}$ $(n = 29)$ under control conditions (**Figure 4A**). Replicating the behavior of the gating force, the gating-swing change displayed a strong negative correlation with the transepithelial current for currents $I \geq I_C$ (Pearson correlation $r = -0.86$; p-value $= 7 \cdot 10^{-11}$; $n = 34$) and dropped to undetectable levels for $I \leq I_C$ (Figure 4B). For $I \geq I_C$, the gating swing d could reach a value of up to about $8\ \mathrm{nm}$ in the presence of a negative endolymphatic potential or, conversely, be as small as $2\ \mathrm{nm}$ upon application of a potential of opposite polarity.

2.3 The transition between states of strong and weak gating force shows hysteresis

To further explore the transition between states of strong and weak gating force (Figure 2D and Figure 3C), we applied ramps of transepithelial current (**Figure 5A**) while the hair bundle was subjected to triangular mechanical stimulation (Figure 5B). This stimulation protocol allowed to monitor, continuously for the same hair bundle, how the mechanical properties varied as a function of the transepithelial current. The ramps were slow enough that the transepithelial current varied by only ~0.2 μA over the time required to measure a force-displacement cycle (see Experimental Section). Because this variation was too small to elicit a significant variation of the gating force (Figure 3D), the mechanical measurements were quasi static. The mechanical stimulus elicited a force-displacement cycle with clockwise circulation, corresponding to energy dissipation.[8] The cycle displayed a region of lower slope—gating compliance—on the positive and negative half cycles (Figure 5C), where the channels opened and closed, respectively. In addition, the height of the force-displacement cycle was larger within the region of channel gating. This property was previously shown to result from the contribution of the transduction channels' gating force to hair-bundle friction, a phenomenon called gating friction, and the displacement at which the cycle had a maximal height (abscissa of disks in Figure 5C) was identified as the set-point deflection X_0.[8] In the following, the

225 maximal half-height of the cycle, ϕ_{MAX}, was used as a reporter for the magnitude of the gating
226 force.

227 As the transepithelial current decreased from zero to negative values, the region of gating
228 compliance and gating friction in the force-displacement cycle shifted toward more negative
229 displacements, corresponding to a decrease of the set-point deflection and thus opening of the
230 transduction channels (Figure 5C, movie S1, Supplementary Information). Following the point
231 of inversion symmetry in a force-displacement cycle resulted in a nearly linear trajectory of
232 slope $0.4 \pm 0.2\ \mathrm{pN \cdot nm^{-1}}$ ($n = 8$; Figure 5D). In addition, the height of the force-
233 displacement cycle, and thus the maximal friction force ϕ_{MAX} increased before saturating
234 (Figure 5E). When the absolute magnitude of the negative current became large enough,
235 corresponding to $I \leq I_C = -3.7 \pm 1\ \mu\mathrm{A}$ and an endolymphatic potential $U \leq U_C \simeq -37 \pm$
236 $10\ \mathrm{mV}$ ($n = 8$), the friction force ϕ_{MAX} dropped (Figure 5E, F and movie S1, Supplementary
237 Information) until the nonlinearity vanished (Figure 5C, red). These observations on single hair
238 cells (solid line in Figure 5E) mirrored the measured changes of the gating force upon
239 application of a static transepithelial current in an ensemble of cells (Figure 3C). We note that
240 gating friction generally depends on the activation time of the transduction channels, not just
241 on the gating force.[8] Detailed analysis of the force-displacement cycles suggests that the
242 channel-activation time had increased by about 50%, on average, when the friction force ϕ_{MAX}
243 reached a saturating value upon application of a negative transepithelial current (Figure S3,
244 Supplementary Information). The observed variation of hair-bundle friction (Figure 5E,F) thus
245 resulted from modulation of both the channel-activation time and the gating force (Figure 3C).

246 The polarity of the current ramp was then reversed. As the negative current increased, the
247 set-point deflection increased and the point of inversion symmetry in the force-displacement
248 cycle showed a nearly linear trajectory of slope $0.6 \pm 0.2\ \mathrm{pN \cdot nm^{-1}}$ ($n = 8$; Figure 5C and
249 D). In addition, the signatures of gating compliance and gating friction, associated to nonlinear
250 force-displacement relations, were retrieved. However, as shown respectively in subpanels (v)
251 and (iii) of Figure 5C, the gating force could remain weak on the ascending ramp at current
252 values where the gating force was strong on the descending ramp. Accordingly, the relation
253 between the friction force ϕ_{MAX} and the transepithelial current I displayed hysteresis
254 (Figure 5E). Over an ensemble of $n = 8$ cells, the transition from a regime of strong to a regime
255 of weak gating force and its reversal were shifted by $2.3 \pm 0.8\ \mu\mathrm{A}$, corresponding to a difference
256 of about 20 mV difference in endolymphatic potential.

2.4 The transition kinetics between the two states occurs on a sub-second timescale

To characterize the kinetics of the transition between states of strong and weak gating force, we applied large negative steps of transepithelial current, here $I = -8\ \mu\text{A}$ (**Figure 6**), while continuously measuring a hair bundle's force-displacement cycle in response to triangular mechanical stimulation. As expected from the effects of current ramps (Figure 5), the force-displacement cycle shifted in the negative direction along the displacement axis and the force-displacement cycle lost the signatures of gating compliance and gating friction (Figure 6A, movie S2, Supplementary Information). The time courses of the average hair-bundle position on the cycle, denoted $\bar{X}$ in the following, and of the maximal friction force ϕ_{MAX} were quantified by measuring the $10 - 90\%$ decay and rise times following the onset and offset of the current step, respectively. Over an ensemble of $n = 4$ hair cells, the characteristic time, $\tau_X^{ON} = 500 \pm 50$ ms, of negative hair-bundle motion evoked by the current step was fivefold longer than that, $\tau_X^{OFF} = 100 \pm 30$ ms, necessary to return to the initial position after the current was turned off (Figure 6B). The friction force ϕ_{MAX} showed an opposite behavior: its decay time, $\tau_\Phi^{ON} = 180 \pm 40$ ms, after the onset of the current step was twofold shorter than its rise time, $\tau_\Phi^{OFF} = 400 \pm 100$ ms, during recovery (Figure 6B). Note that the time required to measure a force-displacement cycle was here of only 20 ms. This duration was about ten times shorter than $\tau_\Phi^{OFF/ON}$ and thus short enough to ensure a quasistatic assessment of hair-bundle mechanics (Experimental Section).

There was thus a separation of timescales between the changes of $\bar{X}$ and ϕ_{MAX}. At the onset of the current step, gating compliance vanished before the negative shift had completed: $\tau_\Phi^{ON}/\tau_X^{ON} = 0.37 \pm 0.17$ (Figure 6B,C). In contrast, after the external transepithelial current was turned off, the mechanical nonlinearity recovered more slowly than the average position of the hair bundle: $\tau_\Phi^{OFF}/\tau_X^{OFF} = 4.2 \pm 2$ (Figure 6B,C).

2.5 Reducing the endolymphatic Ca^{2+} concentration replicates the effects of a negative endolymphatic potential

A negative endolymphatic potential may have mediated its effects on the gating force by reducing the magnitude of the Ca^{2+} influx through the transduction channels. To test this hypothesis, we used iontophoresis of a Ca^{2+} chelator to reduce the endolymphatic Ca^{2+} concentration near a hair bundle and, in turn, the Ca^{2+} influx through the channels under resting conditions. In response to descending and ascending ramps of iontophoretic current

(**Figure 7A**), or equivalently of Ca^{2+} concentration, we again observed an increase in hair-bundle friction followed by a reversible but hysteretic transition between states of strong and weak gating force (Figure 7B,C , movie S3, Supplementary Information). Repeating the experiments over an ensemble of $n = 8$ cells confirmed the robustness of these effects (Figure 7D) and how they mirrored those observed upon modulation of the endolymphatic potential (Figure 5). In addition, the force-displacement relation of a hair bundle could show strong gating compliance under control conditions but reversibly become linear upon step application of a Ca^{2+} chelator, with no noticeable change in the linear stiffness of the hair bundle (Figure 7E). The same behavior was observed in $n = 7$ hair cells. Thus, enough calcium in endolymph was required for the hair bundle to evince strong gating forces.

3. Conclusion

In this work, we showed that varying the endolymphatic potential reversibly modulates the gating force, thus serving as a control parameter for the mechanosensitivity of the hair cell to minute deflections of its hair bundle. This bioelectric effect is large. The gating force increased continuously by up to twofold upon application of negative potentials of moderate magnitude ($0 \geq U \geq -50$ mV) and conversely, could be reduced by up to 80% of the control value at positive potentials (Figure 3D). A major finding of our study is that the gating force varied because the gating swing varied, with only minor effects on the gating-spring stiffness (Figures 3D and 4).

In addition, the hair cell switched from a state of strong gating force to a state of weak gating force when the endolymphatic potential became more negative than a critical value $U = U_C \simeq -50$ mV (Figures 2D, 3C, 5C and 4E). This observation revealed an unexpected transition between two functional states of the hair bundle—one with low mechanosensitivity and one with high mechanosensitivity: a quiescent state of undetectable gating force in hair-bundle mechanics, which is suggestive of gating swings of about one nanometer or less, and an oscillatory state of strong gating force with gating swings of several nanometers, up to 10 nm. At such negative potentials ($U \leq U_C$), the electromotive force driving the influx of cations through the transduction channels is expected to be greatly reduced. Because reducing the Ca^{2+} concentration near a hair bundle evoked a similar transition (Figure 7), the strong gating forces and large gating swings associated to high mechanosensitivity likely required a resting Ca^{2+} influx through the transduction channels that was large enough.

319 Altogether, the variation of the transduction channels' gating force and the gating swing as
320 a function of the endolymphatic potential was nonmonotonic, indicating that
321 mechanosensitivity is maximal within a limited range of potential and, in turn, of Ca^{2+} influx
322 under resting conditions (**Figure 8**).

323 **3.1 Physiological role of the endolymphatic potential**

324 Like other epithelia, the sensory epithelia that house the hair cells in the vertebrate inner ear are
325 polar tissues that experience a transepithelial potential under natural conditions.[34] This
326 potential generally lies within a range $1 - 10$ mV, except in the mammalian cochlea where the
327 endolymphatic potential can reach $+100$ mV. Remarkably enough, this high value of the
328 endolymphatic potential is associated with a Ca^{2+} concentration in endolymph, about 20 μM,
329 which is about one of order of magnitude lower than in hearing organs from non-mammalian
330 species or than in vestibular organs. Our results on frog saccular hair cells (Figures 3 and 7)
331 raise the possibility that the combination of a large endolymphatic potential and a low Ca^{2+}
332 concentration in the cochlea might maintain a Ca^{2+} influx within the optimal range to allow for
333 large gating forces while boosting the magnitude of transduction currents. In support of this
334 inference, a mechanical nonlinearity attributed to hair-bundle mechanics has been measured in
335 an ex-vivo preparation of the Gerbil cochlea, but only under conditions that replicate a normal
336 endolymphatic potential and Ca^{2+} concentration.[13,35] This nonlinearity disappears when no
337 endolymphatic potential is applied, which makes sense within the framework of our results: the
338 potential is then effectively very negative with respect to natural conditions—by 100 mV,
339 perhaps enforcing a similar state of weak gating force as we report here in frog upon application
340 of a potential that is negative enough (Figure 2D, 3C and 5). Note that immersing the sensory
341 epithelium in artificial perilymph, as is routinely performed in the field, is also expected to lead
342 to weak gating forces but here as a result of a too high Ca^{2+} influx. In the cochlea, the Ca^{2+}
343 concentration in perilymph is indeed nearly two orders of magnitude higher than in endolymph.
344 Our results on frog saccular hair cells thus help putting ex-vivo measurements on mammalian
345 hair cells into perspective. In addition, our observations also imply that a spatial gradient in the
346 endolymphatic potential, as observed in vivo in the mammalian cochlea,[36] might provide a
347 mechanism to tune the gating force and thus mechanosensitivity across hair cells.

348 In our experiments on hair cells from the frog saccule, control conditions approach natural
349 conditions: the top and bottom compartments have ionic compositions that mimic those of
350 endolymph and perilymph, respectively, and there is no transepithelial potential. Also, our

351 approach is based on force measurements, which in contrast to standard electrophysiological
352 approaches does not disrupt the integrity of the hair cell or their internal ionic concentrations.
353 Under these nearly natural conditions, the gating force is strong, as a matter of fact strong
354 enough to evoke negative stiffness, promote spontaneous oscillations of the hair bundle and
355 mechanical amplification of weak periodic stimuli.[9,23,24] We applied endolymphatic potentials
356 within a range of ± 100 mV. While this range departs from natural conditions, pushing the hair
357 cells into uncharted territory disclosed gating-force control by the endolymphatic potential and
358 also indicated that the hair cell operates near an optimum of mechanosensitivity under natural
359 conditions.

360 It is worth noting that the difference in electrical potential between endolymph and the hair-
361 cell interior likely constitutes the relevant control parameter, not the endolymph potential per
362 se. From this perspective, modifying the endolymphatic potential may serve as a proxy for
363 evaluating the effects of varying the hair cell's transmembrane potential—at least insofar as
364 mechanosensitivity of the transduction channels is concerned. The efferent nervous system is
365 known to provide descending feedback from the brain to tune sensitivity of the auditory
366 system.[37] Activation of the efferent system leads to hyperpolarization of the hair cell.[38–40]
367 Assuming that hyperpolarization of the hair cell has similar effects on transduction channels'
368 operation as raising the endolymph potential to more positive values, our work opens the
369 possibility that efferent activation might help desensitize hair cells by reducing the transduction
370 channels' gating force and gating swing (Figure 8). More generally, any perturbation evoking
371 a sustained change of the endolymphatic potential, of the intracellular potential, or of the
372 intracellular calcium concentration near the channels' pore would be expected to affect the
373 gating force and, in turn, hair-cell mechanosensitivity.

374 **3.2 Effects of Ca^{2+} on hair-bundle mechanics**

375 Varying the endolymphatic potential afforded a means to reversibly and robustly control the
376 electric field in the membrane near the transduction channels and in turn the electromotive force
377 that controls the magnitude of transduction currents, including the Ca^{2+} influx into the hair cell.
378 Reducing the Ca^{2+} concentration near a hair bundle resulted in similar effects on gating
379 compliance and gating friction than applying negative endolymphatic potentials (Figure 7).
380 This finding indicates that negative endolymphatic potentials modulated the gating force, at
381 least in part, by reducing the Ca^{2+} influx through the transduction channels, whereas positive
382 potentials do the opposite. We cannot exclude, however, that the endolymphatic potential also

383 directly affected channel gating by mediating an electric force on the transduction-channel
384 protein complex. Depolarization of the hair cell has been previously shown to evoke fast
385 movements of the hair bundle, even with channels blocked and thus with no change in the Ca^{2+}
386 influx though the channels, which may be indicative of a rearrangement of the channel protein
387 complex.[41,42]

388 Calcium has previously been shown to affect the channel activation time, the operating point
389 of the transducer and the kinetics of the active adaptation process that drives active hair-bundle
390 motility.[4,24,26,27,30,31,43,44] Moreover, there is some evidence that the extracellular calcium
391 concentration can modulate the stiffness of the hair bundle.[27,33,45] In our experiments, negative
392 endolymphatic potentials produced effects on spontaneous hair-bundle oscillations (Figure S2,
393 Supplementary Information) that were qualitatively similar as those reported earlier in response
394 to depolarization of the hair cell [41,46] or to a decrease of the Ca^{2+} concentration in
395 endolymph.[26] Conversely, positive endolymphatic potentials produced similar effects as
396 hyperpolarization of the hair cell or increasing the endolymphatic Ca^{2+} concentration.

397 Our findings demonstrate that calcium does more than modulate the operating point of the
398 transducer and the kinetics of channel gating and adaptation: it also affects the magnitude of
399 the gating force. Previous models had postulated stiffer gating springs at lower Ca^{2+},[26,47] in
400 apparent contradiction with recent in-vitro measurements of PCDH15 elasticity.[48] Our
401 observations (Figures 3, 4 and 7) suggest instead that the effect of Ca^{2+} on gating-spring
402 stiffness is small compared to that on the gating swing, at least under our experimental
403 conditions.

404 **3.3 Implications for the mechanism of channel gating**

405 As recognized earlier,[9] we observed that the gating swing (Figure 4) can be nearly one order
406 of magnitude larger than the expected diameter of the transduction channels' pore, which has
407 been estimated at about 1.2 nm.[2] Hair cells thus appear to have implemented a mechanism to
408 magnify the conformational change associated to opening and closing of the transduction
409 channel's pore, a feature also relevant to other mechanosensitive channels.[49] In hair cells, the
410 ion channels that mediate mechanoelectrical transduction are part of a molecular complex that
411 includes TMC1—the pore-forming subunit,[50] TMIE, CIB2, LHFPL5 and the lower end of the
412 tip link, PCDH15.[51,52] In addition, the complex may comprise two copies of each protein,
413 forming a dimeric assembly with an axis of twofold symmetry [53,54] and yielding a total of at
414 least 10 proteins.

There is currently no evidence for a large conformational change in a single component of the transduction complex (e.g. in TMC1, see [55]). However, interactions between the multiple components of the transduction apparatus might lead to a collective rearrangement upon opening of the channel's pore, effectively producing a large gating swing. In this view, the gating swing is not the result of a single conformational change in a single protein—say pore opening in TMC1, but instead of an avalanche of conformational changes in multiple proteins operating in series. In addition, the lipid membrane that houses the transduction-channel protein complex may play a role in the implementation of this effective lever arm on pore opening. Channel gating has been proposed to elicit a membrane-mediated interaction between two channel complexes, each attached to one strand of the PCDH15 dimer, leading to a large movement within the membrane that magnifies the apparent gating swing.[56] Alternatively, as proposed for eukaryotic Piezo channels based on structural evidence,[49] the transduction-channel protein complex may not sit in a flat lipid membrane but instead curve the membrane. A change in membrane deformation upon opening of the channel's pore might then magnify the gating swing.

Whatever the molecular substrate for the gating swing, our work indicates that the transepithelial potential and the extracellular calcium concentration can continuously modulate the magnitude of the movement associated to channel gating when the hair bundle operates in a state of strong gating force and large gating swing (State 1 in Figure 8). In addition, under conditions for which the calcium influx through the channels becomes too low (State 2 in Figure 8), we found that the gating force drops to undetectable levels. The transduction channels have been shown to retain their ability to open and close even when hair cells are depolarized to extreme values, up to +100 mV, [57–59] which, like the very negative endolymphatic potentials applied here, strongly opposes Ca^{2+} entry into the hair cells. In our experiments, the observed transition to a state of weak gating force at endolymphatic potentials $U \leq U_C$ is therefore likely attributable to a drop in the magnitude of the gating swing rather than to a loss of the channels' ability to gate. Our observations suggest that the channel-protein complex must be primed by enough intracellular calcium to elicit a large gating swing.

What could be the mechanisms by which Ca^{2+} modulates the gating swing? Recent evidence opens two attractive possibilities. First, calcium was shown to evoke the dissociation of a cytosolic region of TMC1 from CIB2—the calcium- and integrin-binding protein.[60,61] By promoting a tight interaction between CIB2 and TMC1, low calcium might prevent large gating

447 swings upon opening of the channel's pore and, conversely, that enough intracellular Ca^{2+} is
448 necessary to promote a state of high mechanosensitivity of the transduction channel. Hysteresis
449 upon a continuous back-and-forth variation of the endolymphatic potential (Figure 5) or of the
450 extracellular concentration (Figure 7), and the relatively short timescale of the transition
451 between states of strong and weak gating force (Figure 6) provide further support for the
452 bistability of the channel-protein complex. Calcium modulation of the interaction between
453 CIB2 and TMC1 might contribute to the switch-like behavior of the gating swing (Figure. 8).
454 Second, calcium may also modulate the effective size of the gating swing by affecting the
455 mechanical properties of the lipid membrane that houses the transduction channels.[56,62]
456 Diffusivity of the lipids in the membrane of stereocilia varies with calcium and is modulated
457 by the presence of functional transduction channels.[62,63] These observations are consistent with
458 a dual role of the transduction channels as both ion channels and membrane scramblases,[64]
459 which mediate passive bidirectional movement of lipids between the two leaflets of a biological
460 membrane. Modulation of membrane composition is expected to affect channel gating.[65] In
461 addition, should the membrane play a role in force transmission from the tip link to the
462 channel—a departure from the more widely accepted tether model of channel activation, one
463 would expect high-pass filtering of external forces and, reciprocally, of the mechanical correlate
464 of channel gating. This regulatory mechanism can only lead to underestimates but cannot, by
465 itself, explain the large gating swings reported here. Altogether, calcium-mediated modulation
466 of membrane properties may contribute to the modulability of the gating force and gating swing.
467 To cope with the physical requirements of hearing, hair cells have evolved the ability to
468 respond to sound stimuli that vary over timescales as short as a few tens of microseconds, detect
469 deflections of their hair bundle as small as one nanometer or less, and mediate sharp frequency
470 selectivity over three orders of magnitude of sound frequencies.[66] These unique capabilities
471 rely on a transduction-channel protein complex with a highly intricate molecular composition
472 and architecture.[52,54] Inasmuch that the molecular underpinnings of mechanoelectrical
473 transduction by hair cells remains similar across species and organs, our force measurements
474 on hair bundles from frog saccular hair cells demonstrate that the effective conformational
475 change associated to channel gating—the gating swing—can be modulated over a broad range
476 by varying physiological control parameters. The modulability of the gating swing provides a
477 mechanism to tune passive and active mechanosensitivity of the hair cell while maintaining the
478 molecular composition of the transduction channels. Elucidating the molecular rearrangement

479 associated to channel gating and how it can be modulated remain major challenges for future
480 studies.
481

4. Experimental Section

Experimental preparation: All experimental procedures were approved by the Ethics committee on animal experimentation of the Institut Curie; they complied with the European and French National Regulation for the Protection of Vertebrate Animals used for Experimental and other Scientific Purposes (Directive 2010/63; French Decree 2013–118). Details of the experimental preparation have been published elsewhere.[26,27] Briefly, an excised preparation of the frog's saccule (Rivan 92 [67]) was glued with tissue-compatible surgical glue (Histoacryl, B. Braun) over a ~1 mm hole in a plastic disk (Figure 1A). The preparation was then secured in a two-compartment chamber, which exposed the apical and basal aspects of the sensory tissue to fluids with different ionic compositions to mimic physiological conditions. The basal bodies of the hair cells were bathed in artificial perilymph, a standard saline solution containing (in mM): 110 NaCl, 2 KCl, 1.5 $CaCl_2$, 3 D-glucose and 5 Hepes. Hair bundles instead projected into artificial endolymph with (in mM): 2 NaCl, 118 KCl, 0.25 $CaCl_2$, 3 D-glucose, and 5 Hepes. Each solution had a pH of ~ 7.3 and an osmotic strength of $\sim 225\ \mathrm{mmol \cdot kg^{-1}}$. To disconnect the hair bundles from the overlying otolithic membrane, the apical surface of the preparation was exposed for 20 min to endolymph supplemented with $67\ \mu\mathrm{g \cdot mL^{-1}}$ of the protease subtilisin (type XXIV, Sigma). The otolithic membrane was then peeled off to obtain access to individual hair bundles. Experiments were performed at a temperature of 20°C.

Microscopic apparatus and mechanical stimulation: The preparation was viewed through a $\times 60$ water-immersion objective of an upright microscope (BX51WI, Olympus). The mechanical properties of single hair bundles were characterized using published methods.[8,27] In short, the tip of a stimulus fiber was affixed to the kinociliary bulb of an individual hair bundle and imaged at a magnification of $\times 944$ onto a displacement monitor comprising a dual photodiode. Stimulus fibers were fabricated from borosilicate capillaries (TW120-3, World Precision Instrument) and coated with a thin layer of gold-palladium to enhance contrast (Hummer 6.1, Anatech ltd.). The fiber was secured by its base to a stack-type piezoelectric actuator (PA-8/14, Piezosystem Jena) driven by a custom-made power supply (Elbatech). Its stiffness, k_F, was estimated from the analysis of thermal fluctuations at the fiber's tip.

In a first stimulation protocol, a series of step displacements, Δ, was applied to the fiber's base. The standard protocol consisted in the application of 7 to 9 successive pairs of step displacements in opposite directions with a magnitude growing with a constant increment,

513 within the range $20 - 40$ nm. The force, $F = k_F\ (\Delta - X)$, and the bundle's displacement, X,
514 were estimated $5\ -\ 9$ ms after the stimulus onset. This time was long enough for the open
515 probability of the transduction channels to have reached a new steady state and for the frictional
516 contribution to the applied force to have vanished, but short enough to limit the effect of
517 adaptation. The resulting force-displacement relation, $F(X)$, was fitted by the equation [5,24]:

$$F = KX - F_G/[1 + \exp(-(X - X_0)/\delta)] + F_\emptyset, \quad (1)$$

518 from which we estimated the bundle's linear stiffness, K, the gating force, F_G, for the whole
519 hair bundle, and the set-point deflection, X_0. The parameter $F_\emptyset$ ensured that $F = 0$ at $X = 0$.
520 Because we did not use displacement-clamp feedback to stabilize positions of negative
521 stiffness,[9] the characteristic displacement, δ, could not be exploited. In this protocol, both
522 photodiode and command signals were acquired and generated at a sampling rate of 2.5 kHz
523 and the half-power frequency of the lowpass filter was fixed at 1 kHz. A force-displacement
524 relationship was obtained by averaging 7 to 15 repetitions of the same stimulation protocol,
525 which collectively took 10 to 20 seconds.

526 In a second stimulation protocol, we applied a symmetric triangular waveform of motion to
527 the fiber's base, at a frequency of either 40 Hz or 100 Hz and with a peak-to-peak amplitude
528 within the range $600 - 1000$ nm. The force applied to the hair bundle was estimated using a
529 detailed description of the fiber's vibrational modes.[8] This protocol resulted in force-
530 displacement cycles with counterclockwise circulation. The half-height at any position, X, in
531 the cycle provides an estimate of the average friction force $\phi(X) = [F^+(X) - F^-(X)]/2$
532 impeding the hair bundle motion at this position, where $F^\pm(X)$ represents the force in the
533 positive and negative half cycle of stimulation, respectively. The friction force displayed a
534 maximum, $\phi_{\mathrm{MAX}} = \phi(X_0)$, at a displacement that was identified earlier as the set-point
535 deflection X_0 in Equation 1.[8] The force-displacement cycle also displayed a point of inversion
536 symmetry of coordinates $(X_0,\ F_0 = [F^+(X_0) + F^-(X_0)]/2)$. The shift, ΔX, between the
537 positions where the hair-bundle speed reached a maximal value, $|dX/dt| = V_{MAX}$, in the
538 positive and negative half cycle of stimulation provided an estimate of the activation time of
539 the transduction channels, $\tau = \Delta X/(2V_{MAX})$.[8] In this protocol, the force-displacement cycle
540 was averaged over ten periods of the triangular stimulus at 40 Hz or, when a fast assessment of
541 hair-bundle mechanics became necessary (as for the data shown in Figure 6), over only two
542 periods of a 100-Hz stimulus. Triangular stimulation thus afforded a means to probe hair-bundle

543 mechanics in a period of time of 20—250 ms, which was 40—1,000 times shorter than the time
544 required to measure a force-displacement relation with the step-stimulation protocol described
545 above. Both photodiode and command signals were acquired and generated at sampling rate of
546 25 kHz. The half-power frequency of the filter was fixed at 12.5 kHz for the photodiode signals
547 and 0.5 kHz for the command signals.

548 *Control of the transepithelial current and potential:* Using a current source (Linear
549 Stimulator Isolator A395, World Precision Instruments) connected to a pair of silver chloride
550 electrodes (Figure 1A), we applied steps of transepithelial current with a magnitude that was
551 varied within a range of ± 10 μA. In some preparations, we measured the transepithelial
552 potential, $U(t)$, evoked by a step of transepithelial current, $I_{STEP} = 1$ μA (Figure 1B), using an
553 additional pair of electrodes connected to the headstage of a differential amplifier (voltage gain
554 $\times 50$; Model 3000, Systems Inc). The time course of the transepithelial potential was well
555 described by an exponential relation $U(t) = U_{MAX} \exp(-t/\tau)$, with a characteristic timescale
556 $\tau = 230 \pm 50$ μs (mean $\pm$ SD, n =13). Over this ensemble of 13 saccules, we found a
557 transepithelial resistance $R = U_{MAX}/I_{STEP} = 10 \pm 2$ kΩ and capacitance $C = 23 \pm 4$ nF,
558 which accords with previous estimates.[22] Thus, over the range of transepithelial currents that
559 we explored, the potential into the artificial endolymph that bathed the hair bundles—the
560 endolymphatic potential— varied within a range of ± 100 mV with respect to the potential in
561 the perilymphatic compartment. In preparations for which we did not measure the
562 transepithelial resistance, the transepithelial potential was estimated by multiplying the applied
563 transepithelial current by the ensemble-averaged resistance given above, thus with a precision
564 of 20%. We note that the tight junctions between hair cells and supporting cells, despite their
565 names, constitute the least resistive element in the equivalent electrical circuit associated to the
566 frog saccule and thus dictate the resistance of the epithelium.[22] The effect of a transepithelial
567 current on the Ca^{2+} and K^{+} influx in to the hair cells is thus thought to be indirect: the
568 transepithelial current produces a transepithelial potential, which in turn affects the magnitude
569 of the electromotive force that drives the ions through the transduction channels.

570 In other experiments, we applied successive ramps of descending and ascending
571 transepithelial currents at an absolute rate within the range of $0.5 - 0.9\ \mu A \cdot s^{-1}$. These rates
572 were low enough to ensure that the variation of the transepithelial current remained small during
573 the time required for probing hair-bundle mechanics, allowing these mechanical measurements

574 to remain quasistatic. The minimal current was maintained for $1 - 2.5$ s before the ascending
575 ramp started.

576 *Iontophoresis of a calcium chelator:* We used iontophoresis of a calcium chelator to decrease
577 the extracellular calcium concentration in the vicinity of individual hair bundles.[15,27] Coarse
578 microelectrodes were fabricated from borosilicate capillaries (TW120F-3, World Precision
579 Instrument) with a pipette puller (P97, Sutter Instrument); their resistance ranged from 0.8 to
580 1.5 MΩ when filled with 3-M KCl and immersed in the same solution. The electrode's tip was
581 positioned at ~3 μm from the hair bundle.

582 In a first series of experiments, the electrodes were filled with 400-μM pentasodium
583 triphosphate. Triphosphate allowed to decrease the calcium concentration while preserving the
584 integrity of the tip links.[27] A holding current of $+10$ nA was continuously applied to counteract
585 the diffusive release of the calcium chelator from the electrode, to which we added either a step
586 or a succession of descending and ascending ramps of iontophoretic current. The steps had a
587 magnitude of varying between -80 nA and-60 nA, while the ramps reached a minimal value
588 between -90 nA and-50 nA. The current varied at the same rate on the descending and
589 ascending ramps, within a range $5 - 8\ \mathrm{nA} \cdot \mathrm{s}^{-1}$, and the minimal current was maintained for
590 $1 - 2$ s before the ascending ramp started.

591 In a second series of experiments, we aimed at disrupting the tip links to evaluate their
592 contribution to hair-bundle stiffness. In this case, the electrode was filled with EDTA at a
593 concentration of 100 mM. We applied current steps of -100 nA on top of a resting current of
594 $+10$ nA. In three cells, reducing the amplitude of the step to about -35 nA allowed to maintain
595 the integrity of the tip links, adding data to those obtained with iontophoresis of triphosphate to
596 evaluate the effects of reducing the calcium concentration on a force-displacement relation.

597 *Signal generation and acquisition:* All signals were generated and acquired under the control
598 of a computer running a user interface programmed with the LabVIEW software (version 2011,
599 National Instruments). Command signals were produced by a 16-bit interface card (PCI-6733,
600 National Instruments). A second 16-bit interface card (PCI-6250, National Instruments)
601 conducted signal acquisition. Sampling rates for signal generation and acquisition varied within
602 the range $2.5 - 25$ kHz. All signals were conditioned with an eight-pole Bessel antialiasing
603 filter (Model 3384, Krohn-Hite Corporation) at a lowpass cut-off frequency set at half the
604 sampling frequency unless otherwise indicated.

Analysis of spontaneous hair-bundle oscillations: Details of the analysis of the spontaneous oscillations have been published elsewhere.[29] Briefly, the displacement, $X(t)$, of an oscillating hair bundle was monitored over a duration of $10 - 30\ s$. The relation between its power spectrum, $C(f)$, and frequency, f, was first smoothed by a moving average with a frequency window of 1 Hz and then fitted by the sum of two Lorentzians

$$\tilde{C}(f) = \frac{A}{(f_0/2Q)^2 + (f - f_0)^2} + \frac{A}{(f_0/2Q)^2 + (f + f_0)^2}. \quad (2)$$

The fit provided values for the quality factor Q, the characteristic frequency f_0, and parameter A, which is related to the root-mean-square magnitude $X_{RMS} = \langle X(t) - \langle X(t)\rangle^2\rangle = \int_{-\infty}^{+\infty} \tilde{C}(f)df = \sqrt{4\pi AQ/f_0}$ of the movement. In cases where it was bimodal, the probability density of hair bundle positions was fitted by the sum of two Gaussian functions. The fractional area under the Gaussian that was centered at a positive position with respect to the mean bundle position provided a functional estimate of the open probability P_O^{SS} of transduction channels at steady state.

Data analysis: Data were analyzed and visualized using MATLAB. Graphs were generated using MATLAB and Adobe Illustrator (Adobe).

Statistical analysis: All numerical results are quoted as mean ± standard deviation (SD) over an ensemble of n independent measurements. Correlations were evaluated using Pearson's correlation test, with a coefficient r that characterizes the sign and strength of correlation and a p-value that determines the statistical significance of the test. A two-tailed paired Student's *t*-test was used to determine whether the difference between the means of two ensembles of paired measurements was statistically significant. G-power analysis ensured that sample sizes were sufficient to achieve at least 90% power at a 5% significance level. Statistical significance was defined as a p-value less than 0.05, with significance levels indicated as $p < 0.05$ (*), $p < 0.01$ (**), $p < 0.001$ (***). The results of statistical tests are listed in Table S2 (Supplementary Information).

Acknowledgements

Funding:

Fondation pour l'Audition grant FPA RD 2020-7 (PM)

Labex Cell(n)Scale grant ANR-11-LABX-0038 (PM)

Labex Cell(n)Scale grant ANR-10-IDEX-001-02 (PM)

Université Paris Sciences et Lettres and doctoral school "Physique en Île-de-France" grant (AJ)

Competing interest:

The authors declare that they have no conflict of interest.

Author Contributions:

P.M. supervised the study. P.M. and A.J. designed the experiments. A.J. and L.S. performed the experiments. A.J. and P.M. analyzed the data and wrote the manuscript.

Data availability statement: All data needed to evaluate the conclusions in the paper are present in the paper and/or the Supplementary Information. Datasets for all the figures in the Main Text and Supplementary Information can be found on Zenodo (https://doi.org/10.5281/zenodo.14452874). Additional data related to this paper may be requested from the corresponding author.

Received: ((will be filled in by the editorial staff))

Revised: ((will be filled in by the editorial staff))

Published online: ((will be filled in by the editorial staff))

References

1. Hudspeth, A. J. (1989). How the ear's works work. *Nature*, *341*(6241), 397–404. https://doi.org/10.1038/341397a0

2. Fettiplace, R., & Kim, K. X. (2014). The physiology of mechanoelectrical transduction channels in hearing. *Physiological Reviews*, *94*(3), 951–986. https://doi.org/10.1152/physrev.00038.2013

3. Martin, P., & Manley, G. A. (2021). Auditory processing by the cochlea. In *Principles of neural science* (McGraw-Hill Education / Medical; 6th edition, pp. 594–624).

4. Corey, D. P., & Hudspeth, A. J. (1983). Kinetics of the receptor current in bullfrog saccular hair cells. *Journal of Neuroscience*, *3*(5), 962-976.

5. Markin, V. S., & Hudspeth, A. J. (1995). Gating-spring models of mechanoelectrical transduction by hair cells of the internal ear. *Annual Review of Biophysics and Biomolecular Structure*, *24*, 59–83. https://doi.org/10.1146/annurev.bb.24.060195.000423

6. Howard, J., & Hudspeth, A. J. (1988). Compliance of the hair bundle associated with gating of mechanoelectrical transduction channels in the bullfrog's saccular hair cell. *Neuron*, *1*(3), 189-199.

7. Ricci, A. J., Crawford, A. C., & Fettiplace, R. (2002). Mechanisms of active hair bundle motion in auditory hair cells. *The Journal of Neuroscience*, *22*(1), 44–52. https://doi.org/10.1523/JNEUROSCI.22-01-00044.2002

8. Bormuth, V., Barral, J., Joanny, J.-F., Julicher, F., & Martin, P. (2014). Transduction channels' gating can control friction on vibrating hair-cell bundles in the ear. *Proceedings of the National Academy of Sciences USA*, *111*(20), 7185–7190. https://doi.org/10.1073/pnas.1402556111

9. Martin, P., Mehta, A. D., & Hudspeth, A. J. (2000). Negative hair-bundle stiffness betrays a mechanism for mechanical amplification by the hair cell. *Proceedings of the National Academy of Sciences USA*, *97*(22), 12026–12031. https://doi.org/10.1073/pnas.210389497

10. Russell, I. J., Kossl, M., & Richardson, G. P. (1992). Nonlinear mechanical responses of mouse cochlear hair bundles. *Proceedings of the Royal Society London B.*, *250*(1329), 217-27. https://doi.org/10.1098/rspb.1992.0152

11. Géléoc, G. S. G., Lennan, G. W. T., Richardson, G. P., & Kros, C. J. (1997). A quantitative comparison of mechanoelectrical transduction in vestibular and auditory hair cells of neonatal mice. *Proceedings of the Royal Society of London. Series B: Biological Sciences*, *264*(1381), 611–621. https://doi.org/10.1098/rspb.1997.0087

12. van Netten, S. M., & Kros, C. J. (2000). Gating energies and forces of the mammalian hair cell transducer channel and related hair bundle mechanics. *Proc. Biol. Sci.*, *267*(1455), 1915–1923. https://doi.org/10.1098/rspb.2000.1230

13. Chan, D. K., & Hudspeth, A. J. (2005). Ca2+ current–driven nonlinear amplification by the mammalian cochlea in vitro. *Nature Neuroscience*, *8*(2), 149–155. https://doi.org/10.1038/nn1385

14. Kennedy, H. J., Crawford, A. C., & Fettiplace, R. (2005). Force generation by mammalian hair bundles supports a role in cochlear amplification. *Nature*, *433*(7028), 880–883.

15. Tobin, M., Chaiyasitdhi, A., Michel, V., Michalski, N., & Martin, P. (2019). Stiffness and tension gradients of the hair cell's tip-link complex in the mammalian cochlea. *eLife*, *8*, e43473. https://doi.org/10.7554/eLife.43473

16. Mecca, A. A., Caprara, G. A., & Peng, A. W. (2022). cAMP and voltage modulate rat auditory mechanotransduction by decreasing the stiffness of gating springs. *Proceedings of the National Academy of Sciences*, *119*(30), e2107567119. https://doi.org/10.1073/pnas.2107567119

17. Beurg, M., Schwalbach, E. T., & Fettiplace, R. (2024). LHFPL5 is a key element in force transmission from the tip link to the hair cell mechanotransducer channel. *Proceedings of the National Academy of Sciences USA*, *121*(3), e2318270121. https://doi.org/10.1073/pnas.2318270121

18. Nam, J.-H., Peng, A. W., & Ricci, A. J. (2015). Underestimated Sensitivity of Mammalian Cochlear Hair Cells Due to Splay between Stereociliary Columns. *Biophysical Journal*, *108*(11), 2633–2647. https://doi.org/10.1016/j.bpj.2015.04.028

19. Peng, A. W., Scharr, A. L., Caprara, G. A., Nettles, D., Steele, C. R., & Ricci, A. J. (2021). Fluid Jet Stimulation of Auditory Hair Bundles Reveal Spatial Non-uniformities and Two Viscoelastic-Like Mechanisms. *Frontiers in Cell and Developmental Biology*, *9*, 725101. https://doi.org/10.3389/fcell.2021.725101

20. Kozlov, A. S., Risler, T., & Hudspeth, A. J. (2007). Coherent motion of stereocilia assures the concerted gating of hair-cell transduction channels. *Nature Neuroscience*, *10*(1), 87–92. https://doi.org/10.1038/nn1818

21. Kozlov, A. S., Baumgart, J., Risler, T., Versteegh, C. P. C., & Hudspeth, A. J. (2011). Forces between clustered stereocilia minimize friction in the ear on a subnanometre scale. *Nature*, *474*(7351), 376–379. https://doi.org/10.1038/nature10073

22. Corey, D. P., & Hudspeth, A. J. (1983). Analysis of the microphonic potential of the bullfrog's sacculus. *J. Neurosci.*, *3*(5), 942-61. https://doi.org/10.1523/JNEUROSCI.03-05-00942.1983

23. Martin, P., & Hudspeth, A. J. (1999). Active hair-bundle movements can amplify a hair cell's response to oscillatory mechanical stimuli. *Proceedings of the National Academy of Sciences USA*, *96*(25), 14306–14311. https://doi.org/10.1073/pnas.96.25.14306

24. Martin, P., & Hudspeth, A. J. (2021). Mechanical frequency tuning by sensory hair cells, the receptors and amplifiers of the inner ear. *Annual Review of Condensed Matter Physics*, *12*(1), 29–49. https://doi.org/10.1146/annurev-conmatphys-061020-053041

25. Martin, P., Hudspeth, A. J., & Julicher, F. (2001). Comparison of a hair bundle's spontaneous oscillations with its response to mechanical stimulation reveals the underlying active process. *Proceedings of the National Academy of Sciences USA*, *98*(25), 14380–14385. https://doi.org/10.1073/pnas.251530598

26. Martin, P., Bozovic, D., Choe, Y., & Hudspeth, A. J. (2003). Spontaneous oscillation by hair bundles of the bullfrog's sacculus. *The Journal of Neuroscience*, *23*(11), 4533–4548. https://doi.org/10.1523/JNEUROSCI.23-11-04533.2003

27. Tinevez, J.-Y., Jülicher, F., & Martin, P. (2007). Unifying the various incarnations of active hair-bundle motility by the vertebrate hair cell. *Biophysical Journal*, *93*(11), 4053–4067. https://doi.org/10.1529/biophysj.107.108498

28. Ramunno-Johnson, D., Strimbu, C. E., Fredrickson, L., Arisaka, K., & Bozovic, D. (2009). Distribution of frequencies of spontaneous oscillations in hair cells of the bullfrog sacculus. *Biophysical Journal*, *96*(3), 1159–1168. https://doi.org/10.1016/j.bpj.2008.09.060

29. Barral, J., Jülicher, F., & Martin, P. (2018). Friction from transduction channels' gating affects spontaneous hair-bundle oscillations. *Biophysical Journal*, *114*(2), 425–436. https://doi.org/10.1016/j.bpj.2017.11.019

30. Hacohen, N., Assad, J. A., Smith, W. J., & Corey, D. P. (1989). Regulation of tension on hair-cell transduction channels: Displacement and calcium dependence. *Journal of Neuroscience*, *9*(11), 3988-3997.

31. Ricci, A. J., Wu, Y. C., & Fettiplace, R. (1998). The endogenous calcium buffer and the time course of transducer adaptation in auditory hair cells. *Journal of Neuroscience*, *18*(20), 8261–8277.

32. Jacobs, R. A., & Hudspeth, A. J. (1990). Ultrastructural correlates of mechanoelectrical transduction in hair cells of the bullfrog's internal ear. *Cold Spring Harbor Symposia on Quantitative Biology*, *55*, 547–561. https://doi.org/10.1101/sqb.1990.055.01.053

33. Marquis, R. E., & Hudspeth, A. J. (1997). Effects of extracellular Ca2+ concentration on hair-bundle stiffness and gating-spring integrity in hair cells. *Proceedings of the National Academy of Sciences USA*, *94*(22), 11923–11928. https://doi.org/10.1073/pnas.94.22.11923

34. Köppl, C., Wilms, V., Russell, I. J., & Nothwang, H. G. (2018). Evolution of endolymph secretion and endolymphatic potential generation in the vertebrate inner ear. *Brain, Behavior and Evolution*, *92*(1–2), 1–31. https://doi.org/10.1159/000494050

35. Alonso, R. G., Gianoli, F., Fabella, B., & Hudspeth, A. J. (2025). Amplification through local critical behavior in the mammalian cochlea. *Proceedings of the National Academy of Sciences*, *122*(29), e2503389122. https://doi.org/10.1073/pnas.2503389122

36. Li, Y., Liu, H., Zhao, X., & He, D. Z. (2020). Endolymphatic Potential Measured From Developing and Adult Mouse Inner Ear. *Frontiers in Cellular Neuroscience*, *14*, 584928. https://doi.org/10.3389/fncel.2020.584928

37. Fuchs, P. A., & Lauer, A. M. (2019). Efferent Inhibition of the Cochlea. *Cold Spring Harbor Perspectives in Medicine*, *9*(5), a033530. https://doi.org/10.1101/cshperspect.a033530

38. Castellano-Muñoz, M., Israel, S. H., & Hudspeth, A. J. (2010). Efferent Control of the Electrical and Mechanical Properties of Hair Cells in the Bullfrog's Sacculus. *PLoS ONE*, *5*(10), e13777. https://doi.org/10.1371/journal.pone.0013777

39. Art, J. J., & Fettiplace, R. (1984). Efferent desensitization of auditory nerve fibre responses in the cochlea of the turtle Pseudemys scripta elegans. *The Journal of Physiology*, *356*(1), 507–523. https://doi.org/10.1113/jphysiol.1984.sp015480

40. Lin, C.-H. J., & Bozovic, D. (2020). Effects of Efferent Activity on Hair Bundle Mechanics. *The Journal of Neuroscience*, *40*(12), 2390–2402. https://doi.org/10.1523/JNEUROSCI.1312-19.2020

41. Meenderink, S. W., Quinones, P. M., & Bozovic, D. (2015). Voltage-mediated control of spontaneous bundle oscillations in saccular hair cells. *Journal of Neuroscience*, *35*(43), 14457–14466. https://doi.org/10.1523/JNEUROSCI.1451-15.2015

42. Cheung, E. L., & Corey, D. P. (2006). Ca2+ changes the force sensitivity of the hair-cell transduction channel. *Biophys J*, *90*(1), 124–139. https://doi.org/10.1529/biophysj.105.061226

43. Wu, Y. C., Ricci, A. J., & Fettiplace, R. (1999). Two components of transducer adaptation in auditory hair cells. *J Neurophysiol*, *82*(5), 2171–2181. https://doi.org/10.1152/jn.1999.82.5.2171

44. Ricci, A. J., Kennedy, H. J., Crawford, A. C., & Fettiplace, R. (2005). The transduction channel filter in auditory hair cells. *The Journal of Neuroscience*, *25*(34), 7831–7839. https://doi.org/10.1523/JNEUROSCI.1127-05.2005

45. Beurg, M., Nam, J.-H., Crawford, A., & Fettiplace, R. (2008). The actions of calcium on hair bundle mechanics in mammalian cochlear hair cells. *Biophysical Journal*, *94*(7), 2639–2653. https://doi.org/10.1529/biophysj.107.123257

46. Bozovic, D., & Hudspeth, A. J. (2003). Hair-bundle movements elicited by transepithelial electrical stimulation of hair cells in the sacculus of the bullfrog. *Proceedings of the National Academy of Sciences*, *100*(3), 958–963. https://doi.org/10.1073/pnas.0337433100

47. Roongthumskul, Y., Fredrickson-Hemsing, L., Kao, A., & Bozovic, D. (2011). Multiple-timescale dynamics underlying spontaneous oscillations of saccular hair bundles. *Biophysical Journal*, *101*(3), 603–610. https://doi.org/10.1016/j.bpj.2011.06.027

48. Villasante, C. M., Deng, X., Cohen, J. E., & Hudspeth, A.J. (2024). Nanomechanics of wild-type and mutant dimers of the inner-ear tip-link protein protocadherin 15. *Proceedings of the National Academy of Sciences USA*, *121*(40), e2404829121. https://doi.org/10.1073/pnas.2404829121

49. Guo, Y. R., & MacKinnon, R. (2017). Structure-based membrane dome mechanism for Piezo mechanosensitivity. *eLife*, *6*, e33660. https://doi.org/10.7554/eLife.33660

50. Pan, B., Akyuz, N., Liu, X.-P., Asai, Y., Nist-Lund, C., Kurima, K., Derfler, B. H., György, B., Limapichat, W., Walujkar, S., Wimalasena, L. N., Sotomayor, M., Corey, D. P., & Holt, J. R. (2018). TMC1 forms the pore of mechanosensory transduction channels in vertebrate inner ear hair cells. *Neuron*, *99*(4), 736-753.e6. https://doi.org/10.1016/j.neuron.2018.07.033

51. Zheng, W., & Holt, J. R. (2021). The mechanosensory transduction machinery in inner ear hair cells. *Annual Review of Biophysics*, *50*(1), 31–51. https://doi.org/10.1146/annurev-biophys-062420-081842

52. Qiu, X., & Müller, U. (2022). Sensing sound: Cellular specializations and molecular force sensors. *Neuron*, *110*(22), 3667–3687. https://doi.org/10.1016/j.neuron.2022.09.018

53. Ge, J., Elferich, J., Goehring, A., Zhao, H., Schuck, P., & Gouaux, E. (2018). Structure of mouse protocadherin 15 of the stereocilia tip link in complex with LHFPL5. *eLife*, *7*, e38770. https://doi.org/10.7554/eLife.38770

54. Jeong, H., Clark, S., Goehring, A., Dehghani-Ghahnaviyeh, S., Rasouli, A., Tajkhorshid, E., & Gouaux, E. (2022). Structures of the TMC-1 complex illuminate mechanosensory transduction. *Nature*, *610*(7933), 796–803. https://doi.org/10.1038/s41586-022-05314-8

55. Akyuz, N., Karavitaki, K. D., Pan, B., Tamvakologos, P. I., Brock, K. P., Li, Y., Marks, D. S., & Corey, D. P. (2022). Mechanical gating of the auditory transduction channel TMC1 involves the fourth and sixth transmembrane helices. *Science Advances*, *8*(28), eabo1126. https://doi.org/10.1126/sciadv.abo1126

56. Gianoli, F., Risler, T., & Kozlov, A. S. (2017). Lipid bilayer mediates ion-channel cooperativity in a model of hair-cell mechanotransduction. *Proceedings of the National Academy of Sciences USA*, *114*(51), E11010–E11019. https://doi.org/10.1073/pnas.1713135114

57. Assad, J. A., Hacohen, N., & Corey, D. P. (1989). Voltage dependence of adaptation and active bundle movement in bullfrog saccular hair cells. *Proc. Natl. Acad. Sci. USA*, *86*(8), 2918-2922. https://doi.org/10.1073/pnas.86.8.2918

58. Peng, A. W., Effertz, T., & Ricci, A. J. (2013). Adaptation of mammalian auditory hair cell mechanotransduction is independent of calcium entry. *Neuron*, *80*(4), 960–972.

59. Corns, L. F., Johnson, S. L., Kros, C. J., & Marcotti, W. (2014). Calcium entry into stereocilia drives adaptation of the mechanoelectrical transducer current of mammalian cochlear hair cells. *Proc Natl Acad Sci U S A*, *111*(41), 14918–14923.

60. Vallone, R., Dal Cortivo, G., D'Onofrio, M., & Dell'Orco, D. (2018). Preferential binding of Mg2+ over Ca2+ to CIB2 triggers an allosteric switch impaired in Usher syndrome type 1J. *Frontiers in Molecular Neuroscience*, *11*, 274. https://doi.org/10.3389/fnmol.2018.00274

61. Wu, S., Lin, L., Hu, Q., Yao, X., Wang, H., Liu, S., Liu, Q., Xi, Y., Lin, Y., Gong, J., Hu, R., Zhan, W., Luo, Y., He, G., Liu, Z., Xiong, W., Wang, Q., Xu, Z., Bai, F., & Lu, Q. (2025). Mechano-electrical transduction components TMC1-CIB2 undergo a Ca2+-induced conformational change linked to hearing loss. *Developmental Cell*, S1534580725000048. https://doi.org/10.1016/j.devcel.2025.01.004

62. George, S. S., Steele, C. R., & Ricci, A. J. (2020). Rat Auditory Inner Hair Cell Mechanotransduction and Stereociliary Membrane Diffusivity Are Similarly Modulated by Calcium. *iScience*, *23*(12), 101773. https://doi.org/10.1016/j.isci.2020.101773

63. Sam George, S., & Ricci, A. J. (2025). Auditory Hair Cell Mechanotransduction Channels Dynamically Shape the Mechanical Properties of Their Membrane Environment. *Advanced Science*, e08268. https://doi.org/10.1002/advs.202508268

64. Ballesteros, A., & Swartz, K. J. (2022). Regulation of membrane homeostasis by TMC1 mechanoelectrical transduction channels is essential for hearing. *Science Advances*, *8*(31), eabm5550. https://doi.org/10.1126/sciadv.abm5550

65. Bavi, N., Cox, C. D., Nikolaev, Y. A., & Martinac, B. (2023). Molecular insights into the force-from-lipids gating of mechanosensitive channels. *Current Opinion in Physiology*, *36*, 100706. https://doi.org/10.1016/j.cophys.2023.100706

66. Hudspeth, A. J., & Martin, P. (2024). The Critical Thing about the Ear's Sensory Hair Cells. *The Journal of Neuroscience*, *44*(44), e1583242024. https://doi.org/10.1523/JNEUROSCI.1583-24.2024

67. Neveu, A. (2009). Suitability of European green frogs for intensive culture: Comparison between different phenotypes of the esculenta hybridogenetic complex. *Aquaculture*, *295*(1–2), 30–37. https://doi.org/10.1016/j.aquaculture.2009.06.027

Supporting Information

Supporting Information is available from the Wiley Online Library or from the author.

Table of content

The inner ear's hair cells rely on mechanosensitive ion channels to convert vibrations of their hair-bundle into electrical signals. We show that varying the electrical potential (U) across the sensory epithelium modulates a key determinant of mechanosensitivity—the gating force (F_G)—by modulating the gating swing (d), ranging from the size of the channels' pore to nearly tenfold larger.

Electrical control of the transduction channels' gating force in mechanosensory hair cells.

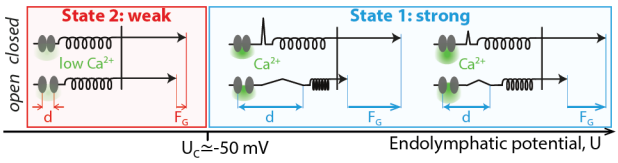

MAIN-FIGURE LEGENDS

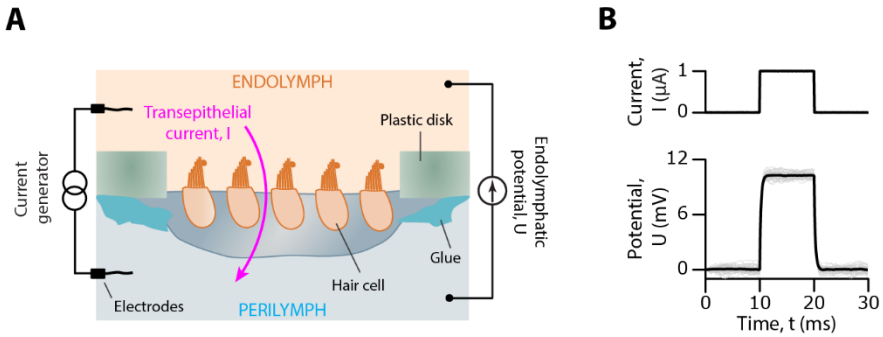

Figure 1: Application of an endolymphatic potential in a two-compartment ex-vivo preparation of the frog saccule. **(A)** Schematic of the setup. The tissue was glued over a 1-mm hole in a plastic disk. Its apical and basal aspects were bathed in artificial endolymph and perilymph, respectively. A transepithelial current, I, was produced by a pair of silver chloride electrodes connected to a current generator, resulting in an endolymphatic potential, U, with respect to the potential in perilymph. The sign convention is such that positive currents lead to a positive value of the endolymphatic potential. **(B)** In this representative example, a +1-μA step of transepithelial current (top) evoked an endolymphatic potential $U \simeq +10$ mV at steady state (bottom, grey), corresponding to a transepithelial resistance of 10 kΩ. An exponential fit (black line), $U(t) = A\exp(-t/\tau)$, to the response yielded the amplitude $A = 10.2$ mV and the characteristic time $\tau = 210$ μs.

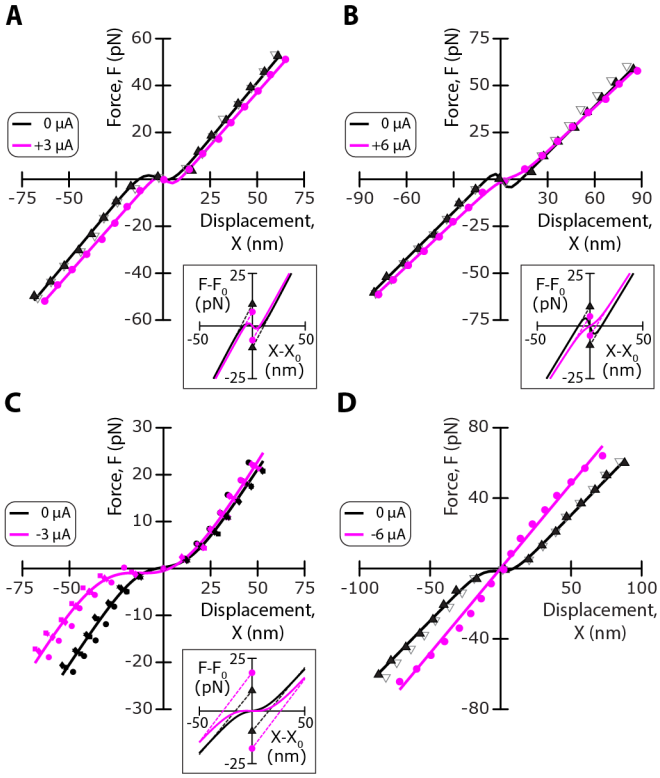

Figure 2 : Representative examples of mechanical changes evoked by a transepithelial current. (A-D) Force-displacement relations, $F(X)$, for four different hair bundles under control conditions ($I = 0$ μA; black) and in the presence of a transepithelial current (magenta) of amplitude $I = +3$ μA (A), $I = +6$ μA (B), $I = -3$ μA (C) and $I = -6$ μA (D). Each relation was fitted by Equation 1 (solid lines; parameter values in Table S1). Insets: the fitted curves are replotted with respect to the origin $(X_0, F(X_0))$, where X_0 is the set-point deflection. Under each condition, the hair bundle's gating force, F_G, was given by the vertical distance between the two symbols in the inset ($I = 0$: triangles; $I \neq 0$: disks). In (A), (B) and (D), the open black symbols correspond to a measurement after restoring control conditions to assess reversibility; in (C), the experiment was repeated 4 times.

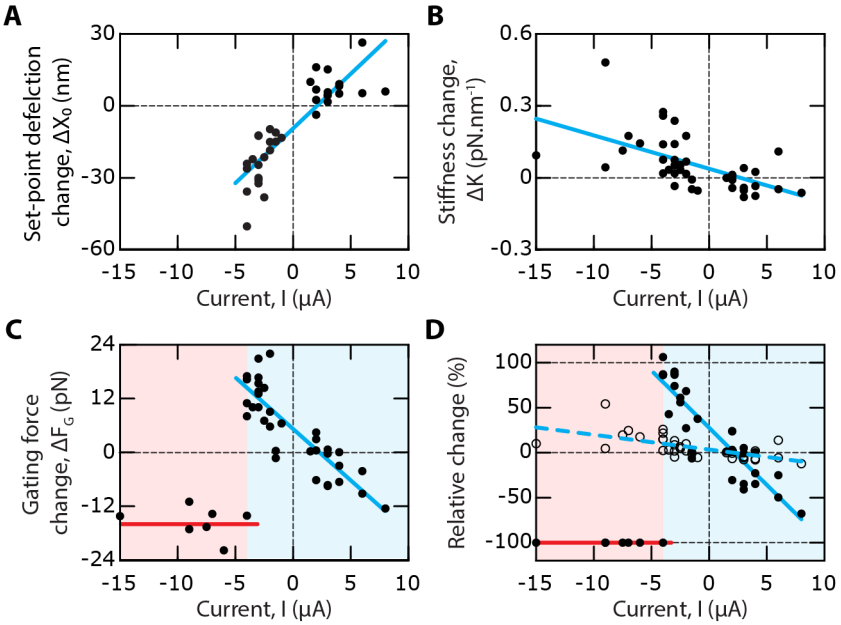

Figure 3 : Changes in set-point deflection, stiffness and gating force upon application of a transepithelial current. **(A)** The change, ΔX_0, of the set-point deflection showed a strong positive correlation to the transepithelial current, I (Pearson correlation r = 0.87; p-value: $4 \cdot 10^{-11}$; $n = 34$). Linear regression (cyan line): ΔX_0 [nm] $= 4.6\, I$ [μA] $- 9.6$ ($R^2 = 0.75$). The set-point deflection could only be measured for I ≥ -5 μA. **(B)** The change, ΔK, of the linear stiffness was negatively correlated to the current (Pearson correlation r $= -0.57$; p-value: 10^{-4}; $n = 41$). Linear regression (cyan line): ΔK [pN . nm^{-1}] $= -0.01\, I$ [μA] $+ 0.04$ ($R^2 = 0.33$) **(C)** For I ≥ -5 μA (cyan area) the change, ΔF_G, of the bundle's gating force showed a strong negative correlation to the current (Pearson correlation r $= -0.86$; p-value: $8 \cdot 10^{-11}$; $n = 34$). Linear regression (cyan line): ΔF_G [pN] $= -2.3\, I$ [μA] $+ 5$ ($R^2 = 0.74$). For I < -5 μA (red area), all the force displacement relations were linear: the gating force had dropped to undetectable levels. Accordingly, the mean value of the change $\Delta F_G = -16 \pm 3$ pN (mean $\pm$ SD, $n = 7$; red line) had an absolute magnitude near that of the gating force, $F_G(I = 0) = 17 \pm 4$ pN (mean $\pm$ SD, $n = 29$) under control conditions. **(D)** Relative change of the hair-bundle's gating force, $\Delta F_G/F_G(0)$ (solid disks) and linear stiffness, $\Delta K/K(0)$ (open disks) as a function of the transepithelial current, I. Linear regressions: $\Delta F_G/F_G(0)$ [%] $= -13 \cdot I$ [μA] $+ 28$ ($R^2 = 0.8$; cyan solid line) and $\Delta K/K(0)$ [%] $= -1.6\, I$ [μA] $+ 3.0$ ($R^2 = 0.32$; cyan dashed line). For $I \leq -5$ μA, $\Delta F_G/F_G(0) = -100$ % (red line).

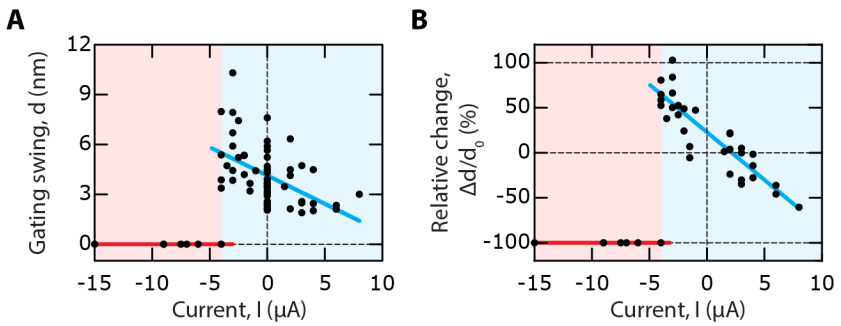

Figure 4: Electrical control of the gating swing. (**A**) For $I \geq -5$ μA (cyan area), the gating swing, d, showed a negative correlation to the transepithelial current, I (Pearson correlation $r = -0.61$; p-value: $1 \cdot 10^{-7}$; $n = 63$). Linear regression (cyan line): $\mathrm{d}\,[\mathrm{nm}] = -0.3 \cdot I\,[\mu A] + 3.3$ ($R^2 = 0.36$). For $\mathrm{I} < -5$ μA (red area), all the force displacement relations were linear: the gating swing had dropped to undetectable levels (red line). Under control conditions ($I = 0$), the gating swing had a mean value $\bar{d}_0 = 3.7 \pm 1.4$ nm (mean $\pm$ SD, $n = 29$). (**B**) For $\mathrm{I} \geq -5$ μA (cyan area) the relative change, $\Delta d/d_0$, of the gating swing where $\Delta d = d(I) - d(I = 0)$ and $d_0 = d(I = 0)$ is plotted as a function of the transepithelial current, I. For $I \geq -5$ μA, the relative change showed a strong negative correlation to the current (Pearson correlation $r = -0.89$; p-value: $3 \cdot 10^{-11}$; $n = 34$). Linear regression (cyan line): $\Delta d/d_0\,[\%] = -11 \cdot I\,[\mathrm{\mu A}] + 22$ ($R^2 = 0.78$). For $\mathrm{I} < -5$ μA (red area), all the force displacement relations were linear: $\Delta d/d_0 = -100\%$ (red line). Same dataset as that used in Figure 3. After each measurement of a bundle's force-displacement relation, the gating swing was estimated as $d = \gamma F_G/(K - K_{SP})$, where F_G and K are respectively the gating force and linear stiffness resulting from a fit of the force-displacement relation with Equation 1 and K_{SP} is the mean stiffness measured over an ensemble of hair bundles after disruption of their tip links. The projection factor $\gamma = 0.14$ was used to estimate the gating swing along the oblique axis of the tip link.

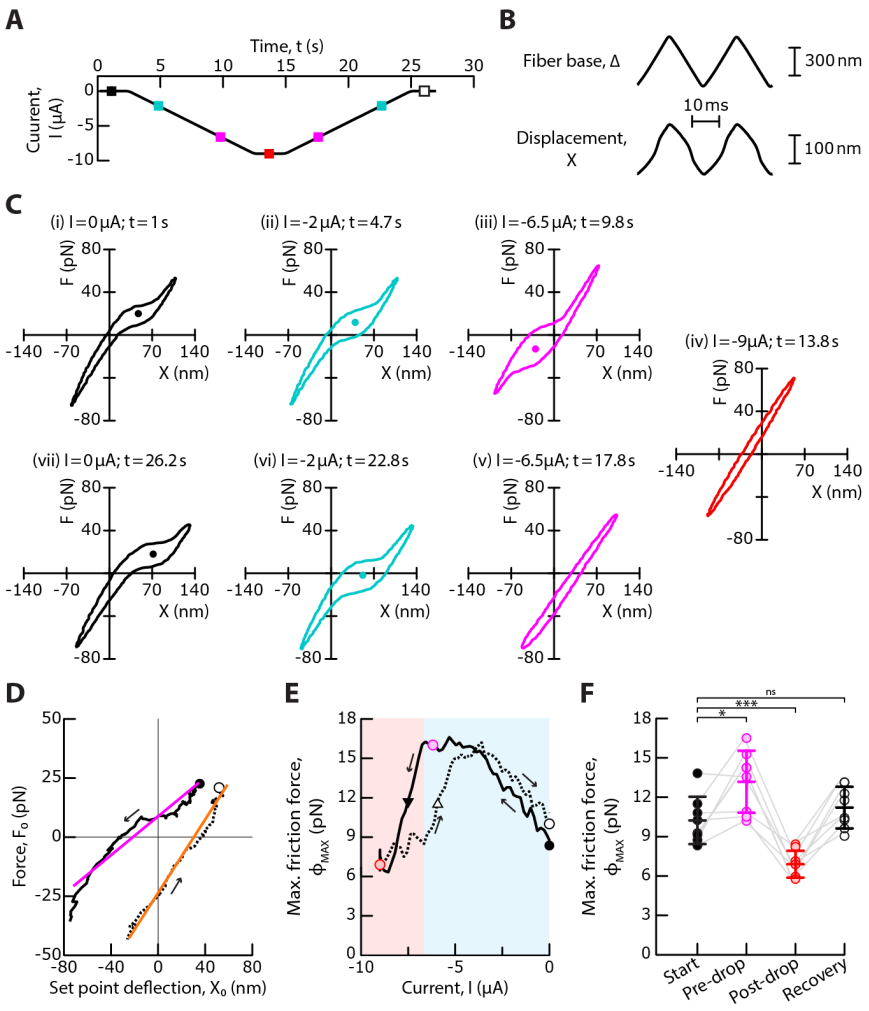

Figure 5 : **Transition between states of strong and weak gating force.** **(A)** A descending ramp of a negative transepithelial current was followed by an ascending ramp of current at the same absolute rate of $0.9\ \mu\text{A} \cdot \text{s}^{-1}$. The colored square symbols indicate the time points of the analysis shown in (C). **(B)** The hair bundle was continuously moved back and forth (bottom) by imposing a periodic triangular movement to the stimulus fiber's base, here with a peak-to-peak amplitude of 600 nm and at a frequency of 40 Hz (top). The movements were averaged over 10 stimulus cycles. **(C)** Force-displacement cycles for the values of the transepithelial current and at times indicated at the top of each sub-panel (see colored square symbols in (A)). **(D)** Trajectory of the point of inversion symmetry (X_0, F_0) in a force-displacement cycle, marked by disks in (C). Linear regressions to these trajectories: $F_0\ [\text{pN}] = 0.41 \cdot X_0\ [\text{nm}] + 9$ ($\text{R}^2 = 0.92$) (magenta) and $F_0\ [\text{pN}] = 0.78 \cdot X_0\ [\text{nm}] + 24$ ($\text{R}^2 = 0.98$) (orange), respectively. **(E)** Maximal friction force, ϕ_{MAX}, as a function of the transepithelial current, I. Blue and red areas delineate regions of strong and weak gating force, respectively. Disks mark

the value of ϕ_{MAX} at the start of the experiment ($I = 0$ μA, black), before ($I = I_{DROP} + 1$ μA with $I_{DROP} = -6.9$ μA, magenta) and after ($I = -9$ μA, red) the drop of ϕ_{MAX}, and at the end of the experiment ($I = 0$ μA, white). Black and white triangles indicate, respectively, the transition from a regime of strong to a regime of weak gating force and its reversal, at half the vertical distance between the magenta and red disks; their abscissas are shifted by 1.7 μA. **(F)** The distributions of ϕ_{MAX} are shown for an ensemble of 8 hair bundles, at the start of each experiment ($I = 0$, black), before ($I = I_{DROP} + 1$ μA, magenta) and after ($I = -9$ μA, red) the drop of ϕ_{MAX}, and at the end of the experiment ($I = 0$ μA, white). The hair bundle transitioned from a state of strong gating force to a state of weak gating force at more negative values of the current than a threshold $I = I_{DROP} = -3.7 \pm 1$ μA (mean $\pm$ SD, $n = 8$). Mean values are shown as horizontal segments and error bars correspond to one standard deviation from the mean. Statistical significance was assessed using a paired t-test with p-values from left to right: $2 \cdot 10^{-2}$, $8 \cdot 10^{-4}$, 10^{-1}. ns $>$ 0.05, * p-value ≤ 0.05, *** p-value ≤ 0.001. In (D-E), black solid and dashed lines correspond to the descending and ascending ramps of transepithelial currents, respectively. Arrows indicate the direction of circulation along the curve from start (black disk) to finish (white disk).

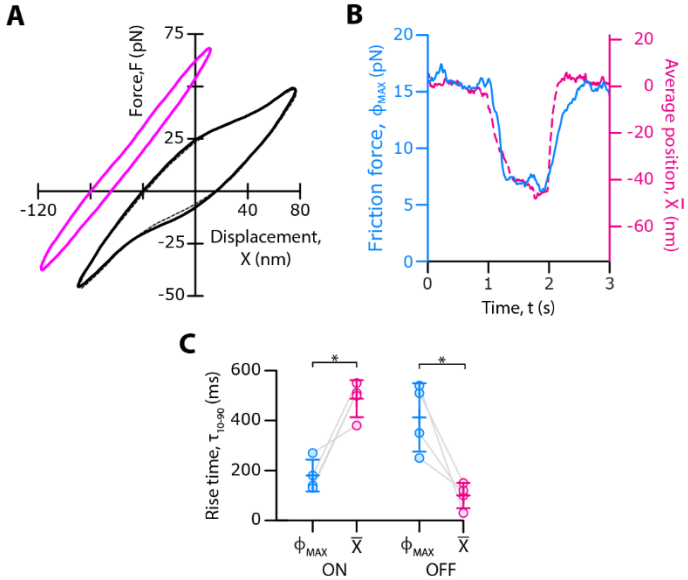

968

969 **Figure 6 : Transition kinetics between states of strong and weak gating force.** **(A)** Force-
970 displacement cycle here averaged over 50 cycles of stimulation, under control conditions ($I =$
971 0; black solid line), 400 ms after the onset of a step of transepithelial current ($I = -8$ µA;
972 magenta) and 600 ms after termination of the current step ($I = 0$; black dashed line). **(B)** Time
973 course of the maximal friction force, ϕ_{MAX}, (blue line) and of the average displacement, $\bar{X}$,
974 (dashed magenta line) in a force-displacement cycle. The current step started at $t = 1$ s and
975 ended at $t = 2$ s. **(C)** For all the 4 different hair bundles that followed the same protocol, time,
976 τ_{10-90}, required for the maximal friction force, ϕ_{MAX} (blue disks), and the average
977 displacement, $\bar{X}$ (magenta disks), to transition from 10% to 90% of the total change after the
978 onset (ON) and the termination (OFF) of a step of transepithelial current ($I = -8$ µA). Mean
979 values are shown as horizontal segments and error bars correspond to one standard deviation
980 from the mean. Statistical significance was assessed using a paired t-test with p-values from
981 left to right: $2 \cdot 10^{-2}$, $3 \cdot 10^{-2}$; * p-value ≤ 0.05. The base of the stimulus fiber followed a
982 periodic triangular waveform of motion, with a peak-to-peak amplitude of 600 nm and at a
983 frequency of 100 Hz. For the data shown in (B) and (C), the force-displacement cycles were
984 averaged over only two cycles of stimulation.
985

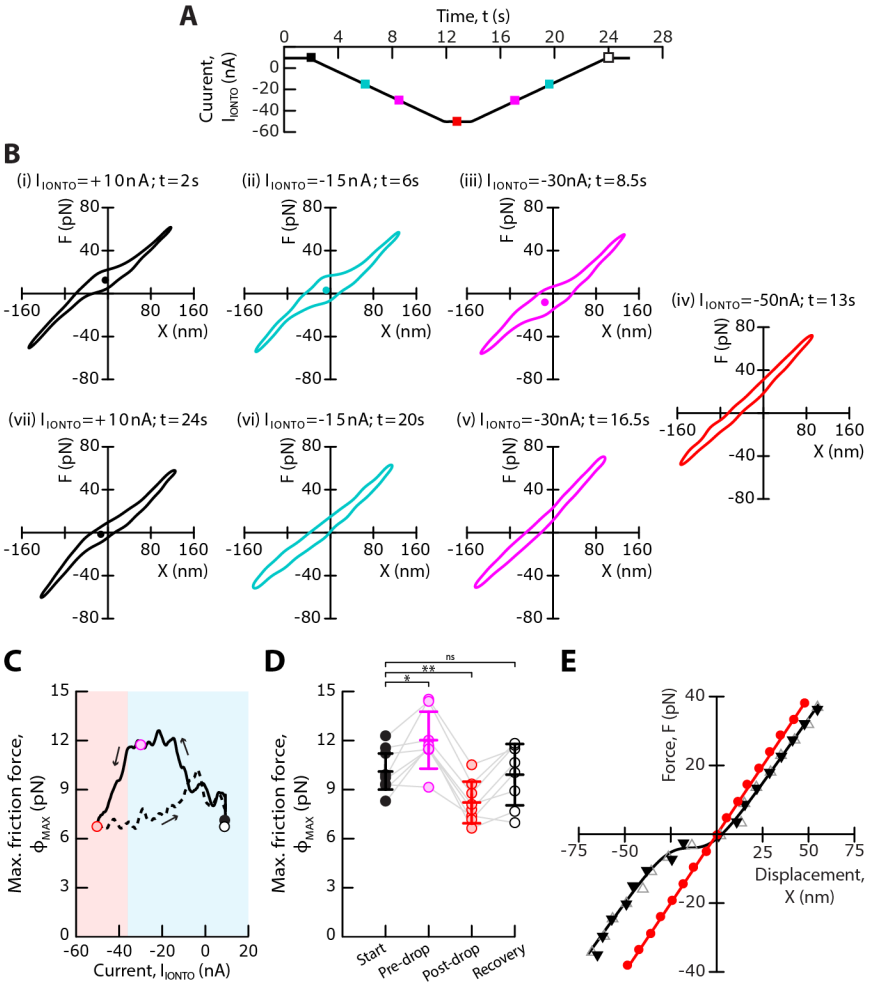

986

987 **Figure 7 : Replicating the effects of negative endolymphatic potentials with iontophoresis**
988 **of a Ca^{2+} chelator.** **(A)** We used iontophoresis of a calcium chelator to decrease the
989 extracellular Ca^{2+} concentration in the vicinity of a hair bundle. A descending ramp of a
990 negative iontophoretic current, I_{IONTO}, which was carried in part by a Ca^{2+}chelator, was
991 followed by an ascending ramp of current at the same absolute rate of $6.6\ \mathrm{nA} \cdot \mathrm{s}^{-1}$. The colored
992 square symbols indicate the time points of the analysis shown in (B). **(B)** Each sub-panel
993 shows the bundle's force-displacement cycle in response to a triangular mechanical stimulus
994 for the value of the iontophoretic current, I_{IONTO}, and at the time, t, indicated at the top. **(C)**.
995 Maximal friction force, ϕ_{MAX}, as a function of the iontophoretic current, I_{IONTO}. Blue and red
996 areas delineate regions of strong and weak gating force, respectively. Disks mark the value of
997 ϕ_{MAX} at the start of the experiment ($I_{IONTO} = +10$ nA, black), before ($I_{IONTO} = I_{DROP} + 5$ nA
998 with $I_{DROP} = -35$ nA, magenta) and after ($I_{IONTO} = -50$ nA, red) the drop of ϕ_{MAX}, and at
999 the end of the experiment ($I_{IONTO} = +10$ nA, white). Arrows indicate the direction of

circulation along the curve. Solid and dashed lines correspond to the descending and ascending ramps of iontophoretic currents, respectively. **(D)** The distributions of ϕ_{MAX} are shown for an ensemble of 8 hair bundles, at the start of the experiment ($I_{IONTO} = +10$ nA, black), before ($I_{IONTO} = I_{DROP} + 5$ nA, magenta) and after ($I_{IONTO} = -50$ nA, red) the drop of ϕ_{MAX}, and at the end of the experiment ($I_{IONTO} = +10$ nA, white). The hair bundle transitioned from a state of strong gating force to a state of weak gating force at more negative values of the current than a threshold $I_{IONTO} = I_{DROP} = -40 \pm 10$ nA (mean $\pm$ SD, $n = 8$). Mean values are shown as horizontal segments and error bars correspond to one standard deviation from the mean. Statistical significance was assessed using a paired t-test with p-values from left to right: $1.5 \cdot 10^{-2}$, $5 \cdot 10^{-3}$, $6 \cdot 10^{-1}$; ns > 0.05; * p-value ≤ 0.05, ** p-value ≤ 0.01. (**E**) The force-displacement relation of a different hair bundle displays a region of gating compliance under control conditions (black triangles) but was linear in the presence of a steady iontophoretic current of -60 nA (red circle). This effect was reversible (grey triangles). Each force-displacement relation was fitted by Equation 1 (solid lines; parameter values in table S1). In (B-D), a periodic triangular waveform of motion was applied to the base of the stimulus fiber, with a peak-to-peak amplitude of 600 nm and at a frequency of 40 Hz. In (E), force-displacement relations were instead measured in response to step displacements at the base of the stimulus fiber (see Experimental Section).

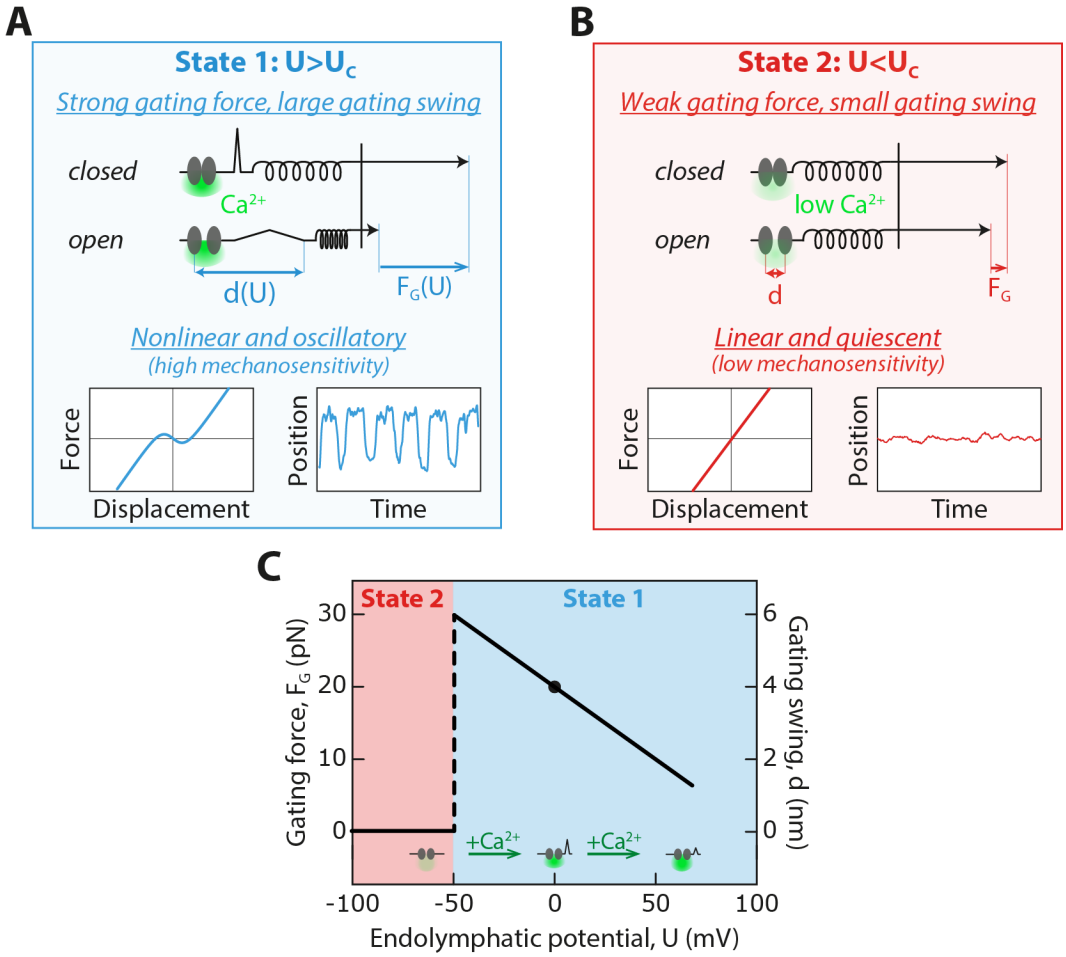

Figure 8 : Conceptual model of electrical gating-force and gating-swing control via intracellular calcium. (**A**) By controlling the electromotive force that drives Ca^{2+} entry, the endolymphatic potential, U, controls the time-averaged intracellular Ca^{2+} concentration near the channels' pore (green halo) as the channels fluctuate between their open and closed states under resting conditions. For endolymphatic potentials, $U \geq U_C$, larger than a critical value, $U_C \simeq -50\ mV$, the intracellular environment is relatively rich in Ca^{2+}, which allows the transduction channels to operate in a state of strong gating force, $F_G(U)$, and large gating swing, $d(U)$. A movement within the transduction-channel protein complex must magnify the small, nanometer-sized, conformational change associated to opening and closing of the channels' pore. In this state—State 1, the hair bundle shows a nonlinear region of strong gating compliance in its force-displacement relation and, in turn, spontaneous oscillations. These active movements have been previously shown to foster frequency-selective amplification of mechanosensitivity to weak periodic stimuli. (**B**) For endolymphatic potentials, $U \leq U_C$, the intracellular ionic environment of the channel is poor in Ca^{2+}. Consequently, the transduction

channels operate in a state of weak gating force and small gating swing—State 2. In this state, the hair bundle is quiescent and endowed with a linear force-displacement relation: there is no detectable signature of channel gating in hair-bundle mechanics, which suggests that the gating swing is less than about one nanometer. Mechanosensitivity in State 2 is much smaller than that in State 1. (**C**) In State 1 (cyan area), the endolymphatic potential, U, continuously and reversibly modulates the magnitude, F_G, of the gating force exerted by the transduction channels on the whole hair bundle (left axis) by changing the channels' gating swing, d (right axis). There is a transition between State 1 and State 2 (red area) at a value of the endolymphatic potential $U = U_C \simeq -50\ mV$. Modulation of the intracellular Ca^{2+} concentration at rest by the endolymphatic potential and its effect on the gating swing is shown schematically at the bottom. Our work suggests that enough intracellular Ca^{2+} is required to prompt large gating forces ($U \geq U_C$; State 1) but that further Ca^{2+} increase results in a continuous decrease of the gating force and gating swing. Under control conditions ($U = 0$, black disks), the transduction channels operate in a state of strong gating force.

Supplementary Information

Electrical control of the transduction channels' gating force in sensory hair cells

Achille Joliot[1,2] , Laure Stickel[1,2] and Pascal Martin[1,2,]*

[1] Physique des Cellules et Cancer, Institut Curie, PSL Research University, CNRS UMR168, F-75248 Paris, France.

[2] Sorbonne Université, F-75252 Paris, France.

[*] Correspondence: pascal.martin@curie.fr

The supplementary information includes:

Tables S1 and S2

Figures S1 to S3

Legends for Movies S1 to S3

Other supporting information for this manuscript includes the following:

Movies S1 to S3

1069 **Supplementary Table**

1070 **Table S1** Parameter values with 95% intervals for fits of force-displacement relations with
1071 Equation 1.

Variable	Definition	Fig. 1A		Fig. 1B		Fig. 1C		Fig. 1D		Fig. 5E	
I (μA)	Transepithelial current	0	+3	0	+6	0	−3	0	−6	n/a	n/a
I_{IONTO} (nA)	Iontophoretic current	n/a	n/a	n/a	n/a	n/a	n/a	n/a	n/a	+10	−60
X_0 (nm)	Set-point deflection	−3 ± 2	1 ± 1	1 ± 2	+6 ± 4	−0.2 ± 0.6	−12 ± 1	−2 ± 3	n/a	−14 ± 3	n/a
K ($\mathrm{pN \cdot nm^{-1}}$)	Stiffness	0.96 ± 0.04	0.91 ± 0.02	0.83 ± 0.03	0.78 ± 0.02	0.61 ± 0.02	0.66 ± 0.03	0.82 ± 0.04	0.96 ± 0.02	0.75 ± 0.07	0.80 ± 0.01
F_G (pN)	Gating force	21 ± 3	13 ± 2	18 ± 3	9 ± 3	19 ± 2	36 ± 3	22 ± 5	n/a	22 ± 7	n/a
δ (nm)	Characteristic length	4 ± 2	2 ± 2	2 ± 7	5 ± 4	9 ± 1	13 ± 1	6 ± 4	n/a	7 ± 4	n/a
$F_\emptyset$ (pN)	Force constant	14 ± 2	5 ± 1	7 ± 2	0.6 ± 1	10 ± 1	25 ± 1	11 ± 2	n/a	18 ± 4	n/a
R^2	Coefficient of determination	0.999	0.994	0.986	0.986	0.986	0.986	0.986	0.986	0.979	0.993

1072

1073

Table S2 Statistical significance and power in two-tailed paired Student's *t*-test.

	Fig. 5F		**Fig. 6C**		**Fig. 7D**	
Number of replicates	$n = 8$ cells in 6 frogs		$n = 4$ cells in 3 frogs		$n = 8$ cells in 6 frogs	
Variable	Max. friction force, ϕ_{MAX} [pN]		Rise time, τ_{10-90} [ms]		Max. friction force, ϕ_{MAX} [pN]	
Test	Start (1) vs Pre-drop (2)	Start (1) vs Pre-drop (2)	Onset:$\phi_{MAX}(1)$ vs $\bar{X}$ (2)	Offset:$\phi_{MAX}(1)$ vs $\bar{X}$ (2)	Start (1) vs Pre-drop (2)	Start (1) vs Post-drop (2)
Mean (1)	10.2	10.2	180	412	10.1	10.1
SD (1)	1.7	1.7	55	118	1.3	1.3
Mean (2)	13.2	12.1	487	100	12.1	8.2
SD (2)	2.2	1.6	64	44.1	1.6	1.19
Effect size	1.7	1.6	5.6	-2.6	1.6	-1.4
Statistical power	0.98	1.00	1.00	0.92	0.97	0.92
p-value	$2 \cdot 10^{-2}$	$1.5 \cdot 10^{-2}$	$1.5 \cdot 10^{-2}$	$1.5 \cdot 10^{-2}$	$1.5 \cdot 10^{-2}$	$5 \cdot 10^{-3}$

Supplementary Figures

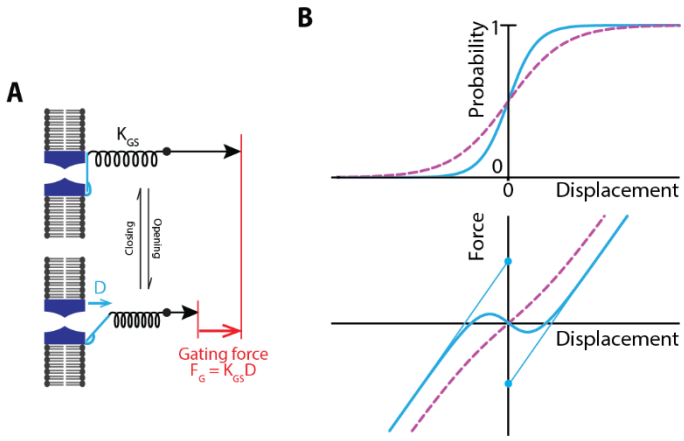

Figure S1 : Gating-spring model of mechanoelectrical transduction. **(A)** The concept of gating force. When the transduction channels switch between their open and closed state, tension in the gating springs is reduced (black arrows); this mechanical correlate of channel gating is called the gating force, $F_G = K_{GS} \cdot D$ (red arrow), where K_{GS} is the combined stiffness of all the gating springs operating in parallel in the hair bundle and D is the gating swing of each channel. **(B)** Electrical and mechanical responses to hair-bundle displacement. Top: sigmoidal relationship of channel open probability to displacement in the case of weak (dashed magenta line) and strong (solid blue line) gating force. The larger the gating force, the steeper the sigmoid and the more sensitive the hair cell is to displacement of its hair bundle. Bottom: The force–displacement relationship displays a shallow nonlinearity when sensitivity is low (dashed magenta curve) and a strong nonlinearity when sensitivity is high (smooth blue curve). The gating force is given by the vertical shift between the two linear limbs of the force-displacement relation; it is here shown in the case of high sensitivity as the distance between the two disks.

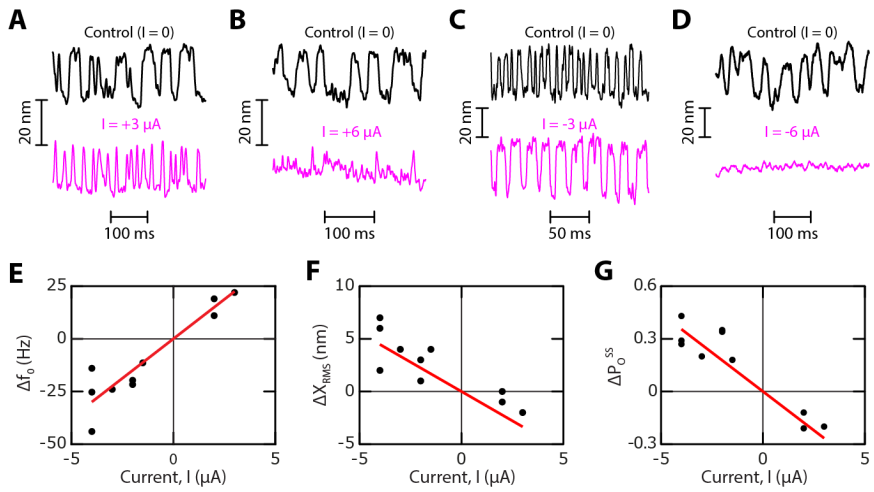

Figure S2 : Effects of a transepithelial current on spontaneous hair-bundle oscillations. Under control conditions ($I = 0$), over an ensemble of $n = 10$ oscillatory hair bundles, the oscillations had a characteristic frequency $f_0 = 22 \pm 14$ Hz, a root-mean-squared (RMS) amplitude $X_{RMS} = 13 \pm 4$ nm and their bimodal position histograms were associated with a steady-state open probability for the transduction channels $P_O^{SS} = 0.4 \pm 0.1$, thus close to $1/2$. These characteristics are remarkably similar to those reported earlier with hair cells from a different frog species.[26,29] **(A-D)** Representative examples of spontaneous hair-bundle oscillations under control conditions ($I = 0$; top) and in the presence of a transepithelial current (bottom) $I = +3$ μA (A), $I = +6$ μA (B), $I = -3$ μA (C), and $I = -6$ μA (D). **(E)** The change, Δf_0, of the oscillation frequency displayed a strong positive correlation to the transepithelial current (Pearson correlation $r = +0.9$; p-value $= 10^{-4}$; $n = 10$). **(F)** The change, ΔX_{RMS}, of the RMS amplitude of spontaneous oscillations displayed a strong negative correlation to the transepithelial current (Pearson correlation $r = -0.9$; p-value $= 1 \cdot 10^{-3}$; $n = 10$). **(G)** The change, ΔP_O^{SS}, of the open probability at steady state displayed a strong negative correlation to the transepithelial current (Pearson correlation r $= -0.9$, p-value $= 1 \cdot 10^{-4}$, $n = 10$). In (A), the transepithelial current evoked an increase of the oscillation frequency from 17 Hz to 39 Hz, a decrease of the RMS amplitude of oscillation from 7 nm to 5 nm and a decrease of the steady-state open probability from 0.5 to 0.3. Conversely in (B), the frequency of oscillation decreased from 49 Hz to 25 Hz, the RMS amplitude of oscillation increased from 11 nm to 15 nm and the steady-state open probability increased from 0.4 to 0.6. In the presence of a large positive current ($I = +6$ μA; panel B), the hair bundle only produced irregular spiky movements in the positive direction: the transduction channels were closed most of the time and evinced brief

openings. Instead, a large negative current ($I = -6\ \mu A$; panel D) completely abolished spontaneous oscillations. Red lines in (E-G) correspond to proportional fits of respective slopes $7\ \mathrm{Hz} \cdot \mu A^{-1}$ ($R^2 = 0.86$; panel E), $-1.1\ \mathrm{nm} \cdot \mu A^{-1}$ ($R^2 = 0.6$; panel F), and $-0.08\ \mu A^{-1}$ ($R^2 = 0.83$; panel G).

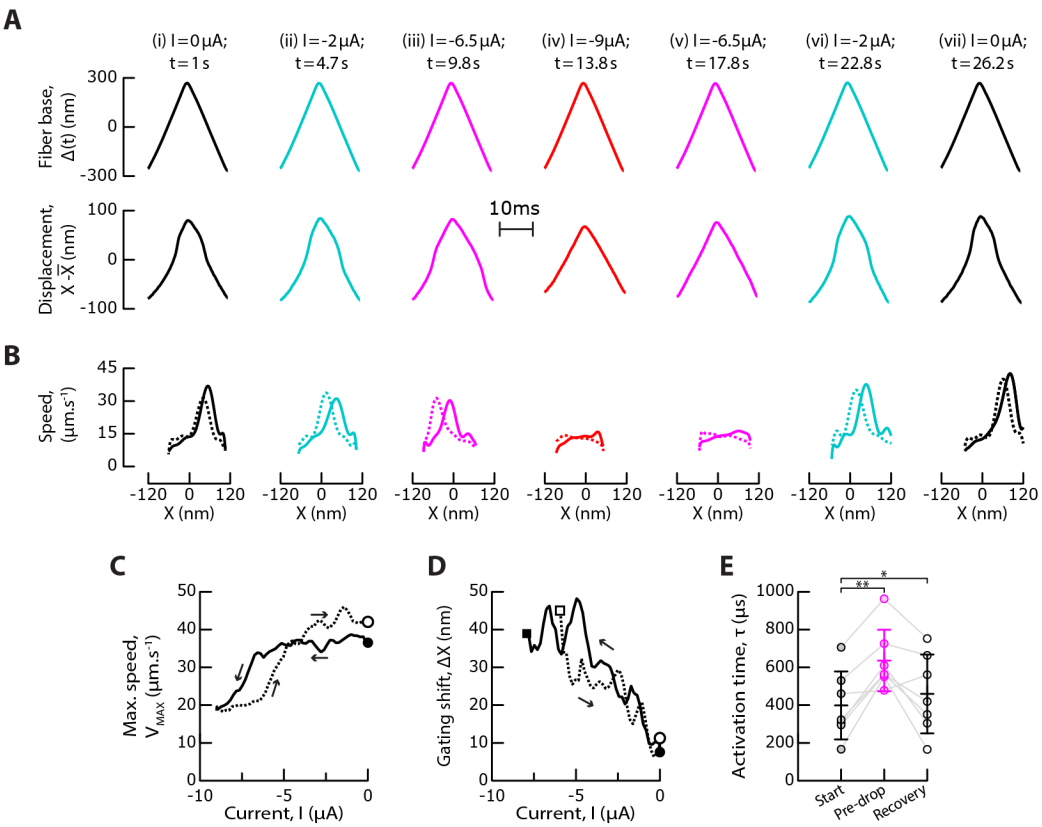

Figure S3 : Effect of a transepithelial current on the channel-activation time. Same data as in Figure 5A-E, to which this figure is associated. The time course of successive ramps of descending and ascending transepithelial current can be found in Figure 5A. **(A)** Fiber-base displacement, Δ (*top*), and hair-bundle displacement, X (*bottom*), as a function of time for one stimulus cycle at time points and values of the transepithelial current indicated at the top of each time trace. **(B)** Hair-bundle speed, $|dX/dt|$, on the positive (*solid line*) and negative (*dashed line*) half cycles of mechanical stimulation as a function of displacement, X. The distance between the two peaks, ΔX, defines the gating shift. **(C-D)** Maximum speed, V_{MAX} (C), and gating shift, ΔX (D), as a function of the transepithelial current, I, which varied in time from start (black disk) to finish (white disk). Arrows indicate the direction of circulation along the curve. Solid and dashed lines correspond to the descending and ascending ramps of transepithelial currents, respectively. In panel (D), a black square indicates the current at which the signatures of gating compliance and gating friction vanished on the descending ramp; bellow this current, the gating shift is no longer defined. Conversely, a white square indicates recovery of the signatures of gating compliance and gating friction on the ascending ramp. **(E)** For the same ensemble of hair bundles as in Figure 5, the distributions of the estimated activation time of the transduction channel, $\tau = \Delta X/(2\,V_{MAX})$, are shown at the start of the

experiment ($I = 0$, black), before the drop of the maximal friction force (magenta, see Figure 5F), and at the end of the experiment ($I = 0$, white). Error bars: mean $\pm$ SD. Statistical significance was assessed using a paired t-test with, from p-values from left to right: $0.0014, 0.021$ *p-value $\leq$ 0.05, **p-value $\leq$ 0.01.

1145

1146 **Legends for supplementary movies**

1147 **Movie S1 (separate file): Transition between states of strong and weak gating force.** Movie
1148 associated to Figure 3A-E. The force-displacement cycle in response to triangular mechanical
1149 stimulation of the hair bundle (top) is shown over time as the transepithelial current follows
1150 successive descending and ascending ramps (bottom). The friction force, $\phi(X)$, at each
1151 displacement X of the hair bundle is color coded as indicated on the right; it is given by the
1152 half-height of the force-displacement cycle. To obtain smooth videos, the force-displacement
1153 cycles were here averaged over 15 cycles, instead of 10 cycles in the data shown in Figure 3.

1154 **Movie S2 (separate file): Kinetics of the transition between states of strong and weak**
1155 **gating force.** Movie associated to Figure 4A-B. The force-displacement cycle in response to
1156 triangular mechanical stimulation of the hair bundle (top) is shown over time before, during
1157 and after application of a negative step of transepithelial current (bottom). The friction force,
1158 $\phi(X)$, at each displacement X of the hair bundle is color coded as indicated on the right; it is
1159 given by the half-height of the force-displacement cycle. The force-displacement cycles were
1160 here averaged over 5 cycles.

1161 **Movie S3 Transition between states of strong and weak gating force upon a decrease of**
1162 **extracellular calcium concentration.** Movie associated to Figure 5A-D. The force-
1163 displacement cycle in response to triangular mechanical stimulation of the hair bundle (top) is
1164 shown over time as an iontophoretic current trough a pipette containing a calcium chelator and
1165 positioned near a hair bundle follows successive descending and ascending ramps (bottom).
1166 The friction force, $\phi(X)$, at each displacement X of the hair bundle is color coded as indicated
1167 on the right; it is given by the half-height of the force-displacement cycle. To obtain smooth
1168 videos, the force-displacement cycles were here averaged over 15 cycles, instead of 10 cycles
1169 for the data shown in Figure 5.

1170